

The role of social ecology in Chiropteran pathogen richness and zoonotic potential

Tim C. D. Lucas

A dissertation submitted in partial fulfillment
of the requirements for the degree of
Doctor of Philosophy
of
University College London.

Centre for Mathematics and Physics in the Life Sciences and Experimental Biology
University College London

May 16, 2015

I, Tim C. D. Lucas, confirm that the work presented in this thesis is my own. Where information has been derived from other sources, I confirm that this has been indicated in the work.

Abstract

My research is about stuff.

It begins with a study of some stuff, and then some other stuff and things.

There is a 300-word limit on your abstract.

Acknowledgements

Acknowledge all the things!

Contents

1	Introductory Material	15
2	Does network structure of bat populations promote viral diversity?	17
2.1	Abstract	18
2.2	Introduction	20
2.2.1	General Intro	20
2.2.2	Specific Intro	20
2.2.3	The gap	22
2.2.4	What I did	23
2.2.5	What I found	23
2.3	Methods	24
2.3.1	Metapopulation model	24
2.3.2	Dispersal	26
2.3.3	Network structure	26
2.3.4	Parameter selection	27
2.4	Results	29
2.4.1	Dispersal	29
2.4.2	Network structure	29
2.5	Discussion	30
2.6	Appendix	31
3	Does ecological and epidemiological seasonality promote viral diversity?	33
4	Does social structure affect viral diversity in wild bat populations?	35
5	gREM for estimating animal density	37
5.1	Abstract	37
5.1.1	1:	37

5.1.2	2:	37
5.1.3	3:	37
5.1.4	4:	38
5.1.5	Keywords	38
5.2	Introduction	38
5.3	Methods	40
5.3.1	Analytical Model	40
5.3.2	Simulation Model	44
5.4	Results	45
5.4.1	Analytical model	45
5.4.2	Simulation model	45
5.5	Discussion	48
5.5.1	Analytical model	48
5.5.2	Accuracy, Precision and Recommendations for Best Practice	49
5.5.3	Limitations	50
5.5.4	Implications for ecology and conservation	51
5.6	Acknowledgments	51
5.7	Data Accessibility	52
6	General Conclusions	53
	Appendices	53
A	gREM Appendix	55
A.1	Table of symbols	56
A.2	Supplementary Methods	57
A.2.1	Introduction	57
A.2.2	Gas model	57
A.2.3	Model SE1	58
A.2.4	Models NE1–3	59
A.2.5	Models SE2–4	61
A.2.6	Model NW1	63
A.2.7	Models NW2–4	64
A.2.8	Model REM	66
A.2.9	Models NW5–7	67

<i>Contents</i>	<i>11</i>
A.2.10 Model SW1–3	69
A.2.11 Model SW4–9	71
A.3 Supplementary Information: Simulation model results of the gREM precision .	75
A.4 Supplementary Information: Impact of parameter error	76
B Colophon	77
Bibliography	77

List of Figures

2.1	The SIR model used.	24
2.2	Network topologies used to test whether network connectedness influences pathogen invasion	27
2.3	Invasion probability	29
5.1	Representation of sensor detection width and animal signal width	40
5.2	Locations where derivation of the average profile \bar{p} is the same	42
5.3	An overview of the derivation of the average profile \bar{p} for the gREM submodel SE2	43
5.4	Expressions for the average profile width	46
5.5	Simulation model results of the accuracy and precision for gREM submodels .	46
5.6	Simulation model results of the accuracy and precision of four gREM submodels	47
5.7	Simulation model results of the accuracy and precision of four gREM submodels	48
A.1	The location of the focal angles $x_{i \in [1,4]}$	57
A.2	Three of the integrals in NE models	59
A.3	The second integral in SE	59
A.4	The second and fourth profiles of NW1	63
A.5	Profile sizes when an animal approaches from behind in models NW2–4	65
A.6	The first profile in SW models	69
A.7	Description of two profiles in SW models	72
A.1	gREM precision given a range of sensor and signal widths	75
A.1	Model sensitivity to error in parameter estimates	76

List of Tables

2.1	Glossary of terms	23
2.2	All symbols used.	31
A.1	List of symbols used to describe the gREM and simulations. ‘-’ means the quantity has no units.	56

Chapter 1

Introductory Material

Some stuff about things. Some more things.

Lorem ipsum dolor sit amet, consectetur adipiscing elit. Etiam lobortis facilisis sem. Nullam nec mi et neque pharetra sollicitudin. Praesent imperdiet mi nec ante. Donec ullamcorper, felis non sodales commodo, lectus velit ultrices augue, a dignissim nibh lectus placerat pede. Vivamus nunc nunc, molestie ut, ultricies vel, semper in, velit. Ut porttitor. Praesent in sapien. Lorem ipsum dolor sit amet, consectetur adipiscing elit. Duis fringilla tristique neque. Sed interdum libero ut metus. Pellentesque placerat. Nam rutrum augue a leo. Morbi sed elit sit amet ante lobortis sollicitudin. Praesent blandit blandit mauris. Praesent lectus tellus, aliquet aliquam, luctus a, egestas a, turpis. Mauris lacinia lorem sit amet ipsum. Nunc quis urna dictum turpis accumsan semper.

Chapter 2

**Does network structure of bat populations
promote viral diversity?**

2.1 Abstract

2.1.0.1 One or two sentences providing a basic introduction to the field

An increasingly large fraction of emerging diseases come from animals and these diseases have a huge impact on human health. The chance that a new disease will come from any particularly wild host species increases with the diversity of pathogens in that species. However, the factors that control pathogen diversity in wild populations are still unknown.

2.1.0.2 Two to three sentences of more detailed background

Host species traits such as population density, longevity, body size and population structure have been shown to correlate with pathogen diversity. However, our mechanistic understanding of how population structure (i.e. non random contacts across the population creating barriers to disease spread) affects pathogen diversity is poor. Greater mechanistic understanding is needed to clarify the exact causal role population structure has in controlling pathogen diversity. Mechanistic models are also likely to be more robust to transferring understanding between taxa and predicting changes.

Typically it is assumed that well-connected populations promote disease spread (high R_0) and therefore promote pathogen diversity. However, if competition is strong endemic pathogens will dominate and prevent new diseases from invading and spreading. In a structured population, stochastic effects could create areas of low prevalence of the endemic disease, allowing new diseases to invade.

We consider bats as a case study as they have been implicated in a number of recent, high profile diseases such as Ebola, SARS, Hendra and Nipah. Bats have varied social structures and so the structure of populations could be one way to prioritise zoonotic disease surveillance in this group.

2.1.0.3 One sentence clearly stating the general problem (the gap)

It is unknown whether population structure allows escape from competition and therefore high diversity.

We hypothesise that low dispersal rates and a low number of connections in a metapopulation network will allow invading pathogens to establish more readily.

2.1.0.4 One sentence summarising the main result

I find that neither population connectedness nor dispersal rate affect the probability that a new pathogen will invade into a population.

2.1.0.5 Two or three sentences explaining what the main result reveals in direct comparison to what was thought to be the case previously

The common assumption that factors causing high R_0 allow new pathogens to invade and therefore increase pathogen diversity is not supported by our study. Instead we find that changes in population structure that would affect R_0 do not affect the probability of invasion of a new pathogen.

2.1.0.6 One or two sentences to put the results into a more general context.

This result means that large scale population structure does not seem to control pathogen diversity. This also implies that population structure is not a useful proxy for pathogen diversity with respect to zoonotic disease surveillance, for example in bats.

2.1.0.7 Two or three sentences to provide a broader perspective,

2.2 Introduction

2.2.1 General Intro

2.2.1.1 Why is pathogen diversity important?

The diversity of pathogens in a wild animal species strongly affects the chance that a disease from that species will infect humans. As over 50% of emerging infectious diseases have an animal source [1], understanding and predicting this process is a global health priority. However, the factors that control the diversity of pathogens in a wild animal population are still unclear.

2.2.1.2 We know some factors that correlate with pathogen diversity

A number of host traits have been shown to correlate with pathogen richness including body size [2], longevity [] and social structure []. However, studies are often contradictory due to small sample sizes, noisy data and because empirical relationships often do not generalise across taxa. Furthermore, the correlation between many traits makes it hard to clearly distinguish which factors are important. Knowing the factors that correlate with pathogen richness also does not tell us how it controls richness. Mechanisms by which a trait could increase pathogen diversity include promoting the evolution of new strains within a species, reduction of the rate of parasite extinction and an increased probability of pathogen invasion.

2.2.1.3 But we do not understand the mechanistic processes

We largely do not understand the mechanisms behind how these traits control pathogen diversity.

2.2.1.4 We cannot assume high R_0 gives high diversity

The processes by which a disease spreads through a population are very well studied. One commonly taken assumption is that factors that promote high disease spread automatically promotes high diversity. However, this ignores competitive mechanisms such as cross-immunity and depletion of susceptible hosts. If competitive mechanisms are strong, then pathogens in populations structured such that R_0 will be high will be able to easily out-compete invading pathogens. If competitive mechanisms are weak, then high R_0 will enable the invasion of new pathogens and allow higher pathogen diversity.

2.2.2 Specific Intro

2.2.2.1 Population structure could be important

One host-species trait that has been largely understudied with respect to pathogen diversity is population structure. Population structure has been comprehensively studied with respect to single or competing epidemics in human populations, wildlife populations and technological

networks. However, as explained above, the assumption that population structures that yield high R_0 will also give high pathogen diversity is unfounded.

The assumption that high R_0 yields high diversity ignores competitive effects. A number of authors have demonstrated a competitive exclusion principle where only the most optimally spreading disease will survive when infection with one pathogen prevents infection with another pathogen [3, 4, 5, 6, 7].

2.2.2.2 Network structure has been studied

Studies of the role of population structure on pathogen diversity have been in very simple systems. These have been so simple that empirical data cannot easily be applied to them to predict pathogen diversity of real wild animal populations. There is a need for models that can be carefully and fully explored, while still capturing the complexities of the real world.

Analytical models have different outcomes for well mixed populations: infinite diversity out competitive exclusion. When competitive exclusion occurs, population structure has sometimes been shown to allow coexistence.

Competing epidemics

[8, 9, 10]

Single pathogen epidemics

2.2.2.3 Empirical evidence that structure might affect diversity

Few studies focus on bats, despite their role in recent zoonoses. Maganga *et al.* found that distribution fragmentation predicts viral richness [11], but [12] finds the opposite relationship. While the data set in [12] is larger, the analysis in [11] is much more focused on fragmentation.

Genetic correlates of population structure have also been used. Turmelle *et al.* [13], in a small analysis, find that high F_{st} (i.e. a structured population) correlates with high richness.

2.2.2.4 Types of population structure

How structured a population is can be defined in many ways on many scales. The most relevant scale is that of an epidemiological population. This is the population within which a pathogen can spread in an epidemiologically relevant time period (years or decades). It is therefore closely related to a population as defined by population genetics, but with movement defined on a shorter time scale.

The epidemiological contacts within the population can be examined at the individual level (as in contact network epidemiology) or larger scales. We consider the metapopulation network the most appropriate. Ignoring the metapopulation assumes a fully mixed population which is unlikely. Trying to study the contact network relies detailed individual level detail

which is not available. Metapopulation models consider a network of small subpopulations. Within subpopulations, epidemiological contacts are fully mixed and relatively fast. Between subpopulations, epidemiological contacts are dependant on an underlying network structure and relatively slow. The network underlying the metapopulation is made up of nodes representing the subpopulations, and edges which represent movement between subpopulations. Animals, and therefore infection, can only move between two subpopulations if they are connected by an edge.

There are two factors that affect how structured a population is, given this model framework. Firstly, dispersal is the rate at which individuals move between subpopulations. Secondly, the metapopulation network structure controls population structure. The simplest measure of how structured the network is the average number of edges each node has. In the extremes, all subpopulations could be either connected to all other subpopulations or only connected to one or two other subpopulations. However, other measures that take into account second-order structure in the network are also often used.

2.2.2.5 Why bats

Bats (Order Chiroptera) have, over the last decade, become a focus for disease research [14, 15]. Recently they have been implicated in a number of high profile diseases such as Ebola, SARS, Hendra and Nipah [14, 16].

2.2.2.6 Describe bats

Bats have an unusual variety of social structures. Group living ranges from colonies 10–1 million [17].

2.2.3 The gap

We have very abstract, simplified models that predict zero or infinite diversity depending on specifics. These cannot be easily applied to real data. they also do not easily predict quantitative or even relative diversity as they often predict either zero or infinite diversity with nothing in between.

We need models that can quantitatively or at least relatively predict diversity in a populations. This requires a middle ground of model diversity.

Furthermore there are few studies that aim to predict bat pathogen diversity. There are no studies that directly model bat pathogen diversity.

Specifically we use these models to test the affects of population structure on the ability of a new pathogen to invade a population. We test two aspects of structure, dispersal rate and connectedness of the metapopulation network.

Term	Definition	Synonyms
<i>Metapopulation</i>	A group of colonies with rare movement of animals between them. Closed to outside migration.	Network
<i>Subpopulation</i>	A group of animals. Social interactions within a colony is likely high.	Node, colony
<i>Dispersal</i>	Movement from one colony to another	Migration
<i>Population</i>	A closed group of animals. No epidemiological affects from outside the group on epidemiological timescale (years – decades.)	
<i>Pathogen diversity</i>	The number of species or strains of pathogens in a host	Pathogen richness
<i>Connectedness</i>		

Table 2.1: Glossary of terms

2.2.4 What I did

I have run epidemiological simulations based broadly on real world bat populations. Although still simplified, the model is complex enough that if good measurements of bat populations could be found, simulations of the real world bat population could be run.

2.2.5 What I found

2.3 Methods

2.3.1 Metapopulation model

2.3.1.1 Two pathogen SIR model

We examine a multipathogen SIR model. This is a compartment model with individuals being classed as susceptible, infected or recovered with immunity (Figure 2.1). Susceptible individuals are counted in class S . There are three infected classes, I_1 , I_2 and I_{12} , being individuals infected with pathogen 1, pathogen 2 or both respectively. Recovered individuals, R , are immune to both pathogens, even if they have only been infected with one. Furthermore, recovery from a pathogen moves an individual straight into the recovered class, even if the individual is infected with both pathogen. This modelling choice allows the model to be easily expanded to included more than two pathogens. The assumption of immediate recovery from all other diseases is likely to be quite accurate for very closely related pathogens as is being studied here as once an acquired immune response is activated, all infections are likely to be cleared quickly.

The coinfection rate is adjusted compared to the first infection rate by a factor α . Birth and death rates are assumed to be equal, $b = d$.

2.3.1.2 Metapopulation

The population is divided into a number of subpopulations. This metapopulation is modelled as a network with subpopulations being nodes and dispersal between subpopulations being indicated by edges (Figure 2.2) Individuals with a subpopulation interact randomly so that the subpopulation is fully mixed. However, dispersal between subpopulations occurs at a rate λ . Individuals can only disperse to subpopulations connected to theirs in the network. The rate of dispersal is not affected by the number of edges a subpopulation has (the degree of the subpopulation). So the dispersal rate from a subpopulation m with degree k_m to subpopulation n is $\frac{\lambda}{k_m}$. Note this rate is independent of the degree of subpopulation n .

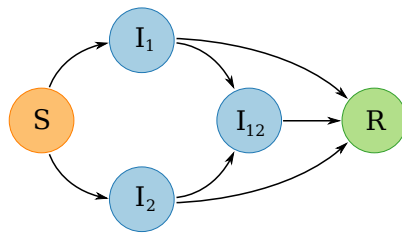


Figure 2.1: The SIR model used.

2.3.1.3 Stochastic simulations

We examine this model using stochastic, continuous time simulations using the Gillespie algorithm. At each step in the simulation we calculate the rate that each possible event might occur. One event is then randomly chosen, weighted by it's rate

$$p(\text{event } i) = \frac{r_i}{\sum_i r_i} \quad (2.1)$$

where r_i is the rate that event i occurs. Finally, the length of the time step, δ , is drawn from an exponential distribution

$$\delta \sim \text{Exp} \left(\sum_i r_i \right). \quad (2.2)$$

This means that the length of each simulation is stochastic. We define the number of events we wish to simulate instead.

We can now write down the rates of all events. I define I_p^+ to be the sum of all classes that are infectious with pathogen p , for example $I_1^+ = I_1 + I_{12}$. Assuming asexual reproduction, that all classes reproduce at the same rate and that individuals are born into the susceptible class we get

$$P(S_{nt'} = S_{nt} + 1) = b \left(S_{nt} + \sum_q I_{qnt} + R_{nt} \right) \quad (2.3)$$

where $P(S_{nt'} = S_{nt} + 1)$ is the probability that the number of susceptibles in subpopulation n will increase by 1 (a single birth) the short time interval t to t' and $\sum_q I_{qnt}$ is the sum of all infection classes $q \in 1, 2, 12$. The rates of death, given a death rate d are given by

$$P(S_{nt'} = S_{nt} - 1) = dS_{nt} \quad (2.4)$$

$$P(I_{qnt'} = I_{qnt} - 1) = dI_{qnt} \quad (2.5)$$

$$P(R_{nt'} = R_{nt} - 1) = dR_{nt}. \quad (2.6)$$

Infection of a susceptible with either pathogen 1 or 2, $S \rightarrow I_p$ where $p \in \{1, 2\}$, is given by

$$P(I_{pnt'} = I_{pnt} + 1, S_{nt'} = S_{nt} - 1) = \beta S_{nt} I_{pnt}^+, \quad (2.7)$$

while coinfection, given a crossimmunity factor α , is given by

$$P(I_{12,nt'} = I_{12,nt} + 1, I_{pnt'} = I_{pnt} - 1) = \alpha\beta I_{nt} I_{pnt}^+. \quad (2.8)$$

The probability of migration from colony m (with degree k_m) to colony n , given a dispersal rate λ is given by

$$P(S_{nt'} = S_{nt} + 1, S_{mt'} = S_{mt} - 1) = \frac{\lambda S_{mt}}{k_m - 1} \quad (2.9)$$

$$P(I_{qnt'} = I_{qnt} + 1, I_{qmt'} = I_{qmt} - 1) = \frac{\lambda I_{qmt}}{k_m} \quad (2.10)$$

$$P(R_{nt'} = S_{nt} + 1, R_{mt'} = R_{mt} - 1) = \frac{\lambda R_{mt}}{k_m}. \quad (2.11)$$

Finally, recovery from any infectious class occurs at a rate γ

$$P(I_{qnt'} = I_{qnt} - 1, R_{nt'} = R_{nt} + 1) = \gamma I_{qnt}. \quad (2.12)$$

In each simulation the population is seeded with 200 infected individuals of disease 1 in each colony. Disease 1 is then allowed to spread and reach equilibrium. After 40,000 events, 10 individuals infected with disease 2 are added to one colony. After another 10,000 events the invasion of disease 2 is considered successful if any individuals with disease 2 still remain.

2.3.2 Dispersal

The values used for the independent variables are chosen to highlight the affects of these variables. Dispersal values are $\lambda = 0.1, 0.01$ and 0.001 dispersals per individual per year. $\lambda = 0.1$ relates to individuals moving between colonies on average twice per lifetime. Therefore exclusively juvenile dispersal would have dispersal rates similar to this. Otherwise it relates to dispersal being a rare event with animals often staying in a colony for many years. $\lambda = 0.01$ relates to 20% of individuals dispersing once in their lifetime. This value is therefore close to male-biased dispersal, with female philopatry. Finally, $\lambda = 0.001$ relates to 2% of individuals dispersing in their lifetime. This therefore relates to a population that does not habitually disperse.

2.3.3 Network structure

The network structure is synthetically created to be either fully or minimally connected (See Figure 2.2). 10 subpopulations was selected as a trade off between computation time and a network complicated enough that structure might have an effect. This value is artificially small compared to wildlife populations.

2.3.4 Parameter selection

The fixed parameters used are chosen to roughly reflect realistic wild bat populations. The death rate d is set as 0.05 per year giving a generation time of 20 years. The birth rate b is set to be equal to d so that the population size is stable. The recovery rate γ is set to 0.1 giving an average infection duration of 10 years. This is therefore a chronic infection. It is very difficult to directly estimate infection durations in wild populations. But it seems that these infections might be long lasting [].

Cross immunity is set to 0.1 so that an individual infected with one disease is 90% less likely to be infected with another. This is a rather arbitrary value. However, the model assumes complete cross immunity after infection. Furthermore, the rationale of the model is that the invading species might be a newly speciated strain of the endemic species. Therefore cross immunity is likely to be very strong.

The population size of each subpopulation is set to 3000. This is appropriate for many bat species [17], especially the large, frugivorous *Pteropodidae* that have been particularly associated with recent zoonotic diseases.

The number of invading pathogens added is set to 10. This is a trade off between getting a reasonable proportion of invasions, while still retaining the stochastic nature of invasion.

Three values of the transmission rate β are used, 2, 5 and 10. All simulations are run under all three transmission rates as this is such a fundamental parameter. Given the recovery, birth and death rates we can calculate an approximation of R_0 that ignores spatial structure. That is, this is R_0 for the local, within-subpopulation dynamics. Furthermore, it is R_0 for the first pathogen; R_0 of the invading pathogen will be lower due to competition. We can calculate that $R_0 \approx \frac{\beta d}{d(d+\gamma)}$. For our three values of $\beta = 2, 5, 10$ we therefore get $R_0 \approx 13.3, 33.3, 66.6$. These

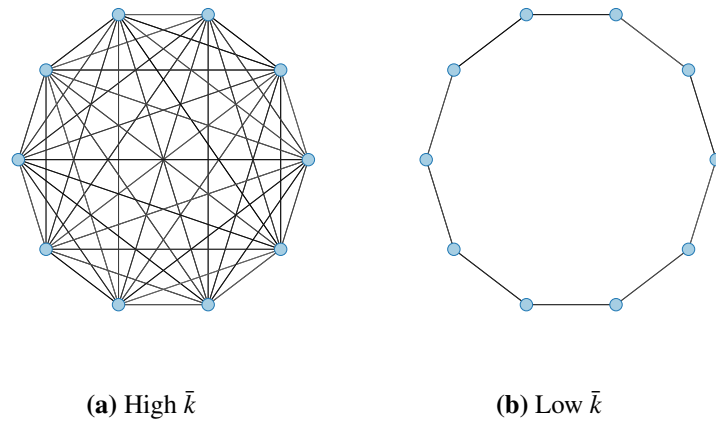


Figure 2.2: The two network topologies used to test whether network connectedness influences a viruses ability to invade. Dispersal is held constant between the two topologies.

values are very high in part to again find a reasonable trade off between the number of simulations and the reasonableness of the parameters. $R_0 \approx 13.3$ is similar to a highly contagious disease such as measles or pertussis.

2.4 Results

2.4.1 Dispersal

The proportion of invasions was not different across dispersal rates. This was true at all transmission levels (χ^2 test. $\beta = 2$: $\chi^2 = 4.19$, $df = 2$, $p = 0.12$. $\beta = 5$: $\chi^2 = 1.27$, $df = 2$, $p = 0.53$. $\beta = 10$: $\chi^2 = 0.01$, $df = 2$, $p = 0.996$)

2.4.2 Network structure

The proportion of invasions was not different between highly connected and largely unconnected metapopulations. This was true at all transmission levels (χ^2 test. $\beta = 2$: $\chi^2 = 0.54$, $df = 1$, $p = 0.46$. $\beta = 5$: $\chi^2 = 0.06$, $df = 1$, $p = 0.81$. $\beta = 10$: $\chi^2 = 3.01$, $df = 1$, $p = 0.08$)

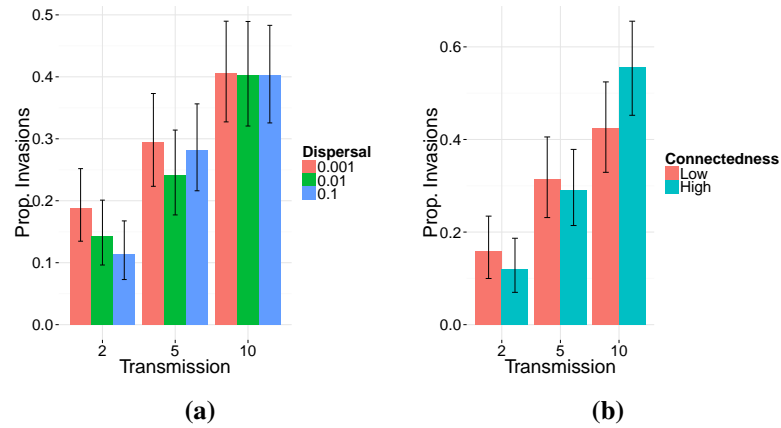


Figure 2.3: The probability of successful invasion. For three different transmission rates, the probability of invasion success does not change between different a) dispersal rates or b) network structures. Error bars are 95% confidence intervals. Other parameters are kept constant at: $N = 10$, $\bar{n} = 3000$, $b = d = 0.05$, $\gamma = 0.1$, $\alpha = 0.1$. When dispersal is varied, the population structure is fully connected. When population structure is varied, $\lambda = 0.01$.

2.5 Discussion

2.6 Appendix

	Explanation	Units	Value
S	Susceptible individuals		
I_q	Infectious with diseases q		
I_p^+	Sum of classes infected with pathogen p		
N	Number of colonies		10
\bar{n}	Mean colony starting size		3000
β	Transmission rate	Transmission events per year per individual	2, 5, 10
γ	Recovery rate	Recovery events per year.	0.1
λ	Dispersal	Dispersal events per day per individual	0.001–0.1
b	Birth rate	Births per year per individual	0.05
d	Death rate	Deaths per year per individual	0.05
d_I	Infectious death rate	Additional deaths per day per individual	
ρ	No. pathogens		2
p	Pathogen index i.e. $p \in \{1, 2\}$ for pathogens 1 and 2		
q	Disease class i.e., $q \in \{1, 2, 12\}$		
\mathcal{N}	Neighbourhood of a node		
t, t'	Time and time plus waiting time i.e., $t + \delta$	Days	
k_i	Degree of node i		
δ	Waiting time until next event	Days	
α	Cross immunity	Proportion	0.1
n, m	Colony index		
A_{mn}	Adjacency matrix.	Distance	
μ	Maximum distance for edge to exist	km	40, 100
σ	Invading pathogen seed size		10
r_i	The rate that event i occurs.	Days ⁻¹	

Table 2.2: All symbols used.

Chapter 3

Does ecological and epidemiological seasonality promote viral diversity?

Lorem ipsum dolor sit amet, consectetur adipiscing elit. Etiam lobortis facilisis sem. Nullam nec mi et neque pharetra sollicitudin. Praesent imperdiet mi nec ante. Donec ullamcorper, felis non sodales commodo, lectus velit ultrices augue, a dignissim nibh lectus placerat pede. Vivamus nunc nunc, molestie ut, ultricies vel, semper in, velit. Ut porttitor. Praesent in sapien. Lorem ipsum dolor sit amet, consectetur adipiscing elit. Duis fringilla tristique neque. Sed interdum libero ut metus. Pellentesque placerat. Nam rutrum augue a leo. Morbi sed elit sit amet ante lobortis sollicitudin. Praesent blandit blandit mauris. Praesent lectus tellus, aliquet aliquam, luctus a, egestas a, turpis. Mauris lacinia lorem sit amet ipsum. Nunc quis urna dictum turpis accumsan semper.

Chapter 4

Does social structure affect viral diversity in wild bat populations?

Lorem ipsum dolor sit amet, consectetur adipiscing elit. Etiam lobortis facilisis sem. Nullam nec mi et neque pharetra sollicitudin. Praesent imperdiet mi nec ante. Donec ullamcorper, felis non sodales commodo, lectus velit ultrices augue, a dignissim nibh lectus placerat pede. Vivamus nunc nunc, molestie ut, ultricies vel, semper in, velit. Ut porttitor. Praesent in sapien. Lorem ipsum dolor sit amet, consectetur adipiscing elit. Duis fringilla tristique neque. Sed interdum libero ut metus. Pellentesque placerat. Nam rutrum augue a leo. Morbi sed elit sit amet ante lobortis sollicitudin. Praesent blandit blandit mauris. Praesent lectus tellus, aliquet aliquam, luctus a, egestas a, turpis. Mauris lacinia lorem sit amet ipsum. Nunc quis urna dictum turpis accumsan semper.

Chapter 5

A generalised random encounter model for estimating animal density with remote sensor data

5.1 Abstract

5.1.1 1:

Wildlife monitoring technology is advancing rapidly and the use of remote sensors such as camera traps and acoustic detectors is becoming common in both the terrestrial and marine environments. Current methods to estimate abundance or density require individual recognition of animals or knowing the distance of the animal from the sensor, which is often difficult. A method without these requirements, the random encounter model (REM), has been successfully applied to estimate animal densities from count data generated from camera traps. However, count data from acoustic detectors do not fit the assumptions of the REM due to the directionality of animal signals.

5.1.2 2:

We developed a generalised REM (gREM), to estimate absolute animal density from count data from both camera traps and acoustic detectors. We derived the gREM for different combinations of sensor detection widths and animal signal widths (a measure of directionality). We tested the accuracy and precision of this model using simulations of different combinations of sensor detection widths and animal signal widths, number of captures, and models of animal movement.

5.1.3 3:

We find that the gREM produces accurate estimates of absolute animal density for all combinations of sensor detection widths and animal signal widths. However, larger sensor detection and

animal signal widths were found to be more precise. While the model is accurate for all capture efforts tested, the precision of the estimate increases with the number of captures. We found no effect of different animal movement models on the accuracy and precision of the gREM.

5.1.4 4:

We conclude that the gREM provides an effective method to estimate absolute animal densities from remote sensor count data over a range of sensor and animal signal widths. The gREM is applicable for count data obtained in both marine and terrestrial environments, visually or acoustically (e.g., big cats, sharks, birds, echolocating bats and cetaceans). As sensors such as camera traps and acoustic detectors become more ubiquitous, the gREM will be increasingly useful for monitoring unmarked animal populations across broad spatial, temporal and taxonomic scales.

5.1.5 Keywords

Acoustic detection, camera traps, marine, population monitoring, simulations, terrestrial

5.2 Introduction

The density of animal populations is one of the fundamental measures in ecology and conservation and has important implications for a range of issues, such as sensitivity to stochastic fluctuations [18] and extinction risk [19]. Monitoring animal population changes in response to anthropogenic pressure is becoming increasingly important as humans rapidly modify habitats and change climates [20]. Sensor technology, such as camera traps [21, 22] and acoustic detectors [23, 24] are widely used to monitor changes in animal populations as they are efficient, relatively cheap and non-invasive, allowing for surveys over large areas and long periods [22, 25, 26]. However, converting sampled count data into estimates of density is problematic as detectability of animals needs to be accounted for [27].

Existing methods for estimating animal density often require additional information that is often unavailable. For example, capture-mark-recapture methods [21, 28] require recognition of individuals, and distance methods [29] require estimates of how far away individuals are from the sensor [30, 31]. When individuals cannot be told apart, an extension of occupancy modelling can be used to estimate absolute abundance [32]. However, as the model is originally formulated to estimate occupancy, count information is simplified to presence-absence data. Assumptions about the distribution of individuals (e.g. a poisson distribution) must also be made [32] which may be a poor assumption for nonrandomly distributed species. Furthermore repeat, independent surveys must be performed and the definition of a site can be difficult, especially for wide-ranging species [33].

The REM method has been successfully applied to estimate animal densities from camera trap surveys [34]. However, extending the REM method to other types of sensors (e.g., acoustic detectors) is more problematic, because the original derivation assumes a relatively narrow sensor width (up to $\pi/2$ radians) and that the animal is equally detectable irrespective of its heading [35].

Whilst these restrictions are not problematic for most camera trap makes (e.g., Reconyx, Cuddeback), the REM cannot be used to estimate densities from camera traps with a wider sensor width (e.g. canopy monitoring with fish eye lenses, [36]). Additionally, the REM method is not useful in estimating densities from acoustic survey data as acoustic detector angles are often wider than $\pi/2$ radians. Acoustic detectors are designed for a range of diverse tasks and environments [25], which naturally leads to a wide range of sensor detection widths and detection distances. In addition to this, calls emitted by many animals are directional [37], breaking the assumption of the REM method.

There has been a sharp rise in interest around passive acoustic detectors in recent years, with a 10 fold increase in publications in the decade between 2000 and 2010 [25]. Acoustic monitoring is being developed to study many aspects of ecology, including the interactions of animals and their environments [37, 38], the presence and relative abundances of species [39], biodiversity of an area [40], and monitoring population trends [26].

Acoustic data suffers from many of the problems associated with data from camera trap surveys in that individuals are often unmarked, making capture-mark-recapture methods more difficult to use [41]. In some cases the distance between the animal and the sensor is known, for example when an array of sensors is deployed and the position of the animal is estimated by triangulation [42]. In these situations distance-sampling methods can be applied [43]. However, in many cases distance estimation is not possible, for example when single sensors are deployed, a situation typical in the majority of terrestrial acoustic surveys [43]. In these cases, only relative measures of local abundance can be calculated, and not absolute densities. This means that comparison of populations between species and sites is problematic without assuming equal detectability [44, 26]. Equal detectability is unlikely because of differences in environmental conditions, sensor type, habitat, and species biology.

In this study, we create a generalised REM (gREM) as an extension to the camera trap model of [35], to estimate absolute density from count data from acoustic detectors, or camera traps, where the sensor width can vary from 0 to 2π radians, and the signal given from the animal can be directional. We assessed the accuracy and precision of the gREM within a simulated environment, by varying the sensor detection widths, animal signal widths, number of captures

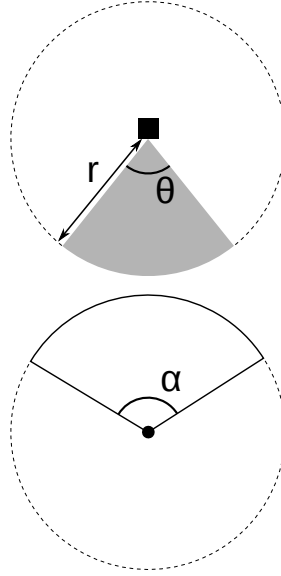


Figure 5.1: Representation of sensor detection width and animal signal width. The filled square and circle represent a sensor and an animal, respectively; θ , sensor detection width (radians); r , sensor detection distance; dark grey shaded area, sensor detection zone; α , animal signal width (radians). Dashed lines around the filled square and circle represents the maximum extent of θ and α , respectively.

and models of animal movement. We use the simulation results to recommend best survey practice for estimating animal densities from remote sensors.

5.3 Methods

5.3.1 Analytical Model

The REM presented by [35] adapts the gas model to count data collected from camera trap surveys. The REM is derived assuming a stationary sensor with a detection width less than $\pi/2$ radians. However, in order to apply this approach more generally, and in particular to stationary acoustic detectors, we need both to relax the constraint on sensor detection width, and allow for animals with directional signals. Consequently, we derive the gREM for any detection width, θ , between 0 and 2π with a detection distance r giving a circular sector within which animals can be captured (the detection zone) (Figure 5.1). Additionally, we model the animal as having an associated signal width α between 0 and 2π (Figure 5.1, see Appendix S1 for a list of symbols). We start deriving the gREM with the simplest situation, the gas model where $\theta = 2\pi$ and $\alpha = 2\pi$.

5.3.1.1 Gas Model

Following [45], we derive the gas model where sensors can capture animals in any direction and animal signals are detectable from any direction ($\theta = 2\pi$ and $\alpha = 2\pi$). We assume that animals are in a homogeneous environment, and move in straight lines of random direction with

velocity v . We allow that our stationary sensor can capture animals at a detection distance r and that if an animal moves within this detection zone they are captured with a probability of one; while outside this zone, animals are never captured.

In order to derive animal density, we need to consider relative velocity from the reference frame of the animals. Conceptually, this requires us to imagine that all animals are stationary and randomly distributed in space, while the sensor moves with velocity v . If we calculate the area covered by the sensor during the survey period, we can estimate the number of animals the sensor should capture. As a circle moving across a plane, the area covered by the sensor per unit time is $2rv$. The expected number of captures, z , for a survey period of t , with an animal density of D is $z = 2rvtD$. To estimate the density we rearrange to get $D = z/2rvt$. Note that as z is the number of encounters, not individuals, the possibility of repeated detections of the same individual is accounted for [46].

5.3.1.2 gREM derivations for different detection and signal widths

Different combinations of θ and α would be expected to occur (e.g., sensors have different detection widths and animals have different signal widths). For different combinations θ and α , the area covered per unit time is no longer given by $2rv$. Instead of the size of the sensor detection zone having a diameter of $2r$, the size changes with the approach angle between the sensor and the animal. The width of the area within which an animal can be detected is called the profile, p . The size of p depends on the signal width, detector width and the angle that the animal approaches the sensor. The size of the profile (averaged across all approach angles) is defined as the average profile \bar{p} . However, different combinations of θ and α need different equations to calculate \bar{p} .

We have identified the parameter space for the combinations of θ and α for which the derivation of the equations are the same (defined as sub-models in the gREM) (Figure 5.2). For example, the gas model becomes the simplest gREM sub-model (upper right in Figure 5.2) and the REM from [35] is another gREM sub-model where $\theta < \pi/2$ and $\alpha = 2\pi$. We derive one gREM sub-model SE2 as an example below, where $2\pi - \alpha/2 < \theta < 2\pi$, $0 < \alpha < \pi$ (see Appendix S2 for derivations of all gREM sub-models). Any estimate of density would require prior knowledge of animal velocity, v and animal signal width, α taken from other sources, for example existing literature [47, 48]. Sensor width, θ , and detection distance, r would also need to be measured or obtained from manufacturer specifications [49, 50].

5.3.1.3 Example derivation of SE2

In order to calculate \bar{p} , we have to integrate over the focal angle, x_1 (Figure 5.3a). This is the angle taken from the centre line of the sensor. Other focal angles are possible (x_2, x_3, x_4) and

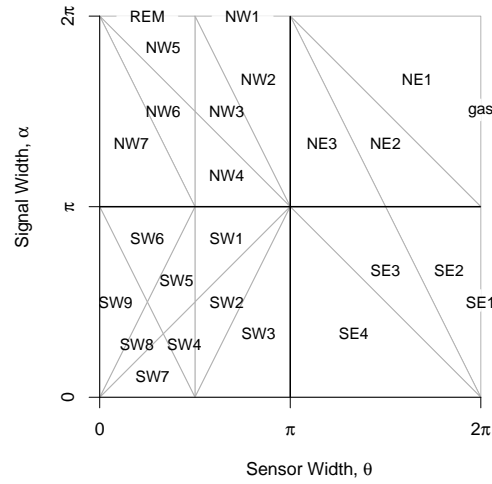


Figure 5.2: Locations where derivation of the average profile \bar{p} is the same for different combinations of sensor detection and animal signal widths. Symbols within each polygon refer to each gREM submodel named after their compass point, except for Gas and REM which highlight the position of these previously derived models within the gREM. Symbols on the edge of the plot are for submodels where $\alpha, \theta = 2\pi$

are used in other gREM sub-models (see Appendix S2). As the size of the profile depends on the approach angle, we present the derivation across all approach angles. When the sensor is directly approaching the animal $x_1 = \pi/2$.

Starting from $x_1 = \pi/2$ until $\theta/2 + \pi/2 - \alpha/2$, the size of the profile is $2r \sin \alpha/2$ (Figure 5.3b). During this first interval, the size of α limits the width of the profile. When the animal reaches $x_1 = \theta/2 + \pi/2 - \alpha/2$ (Figure 5.3c), the size of the profile is $r \sin(\alpha/2) + r \cos(x_1 - \theta/2)$ and the size of θ and α both limit the width of the profile (Figure 5.3c). Finally, at $x_1 = 5\pi/2 - \theta/2 - \alpha/2$ until $x_1 = 3\pi/2$, the width of the profile is again $2r \sin \alpha/2$ (Figure 5.3d) and the size of α again limits the width of the profile.

The profile width p for π radians of rotation (from directly towards the sensor to directly behind the sensor) is completely characterised by the three intervals (Figure 5.3b–d). Average profile width \bar{p} is calculated by integrating these profiles over their appropriate intervals of x_1 and dividing by π which gives

$$\bar{p} = \frac{1}{\pi} \left(\int_{\frac{\pi}{2}}^{\frac{\pi}{2} + \frac{\theta}{2} - \frac{\alpha}{2}} 2r \sin \frac{\alpha}{2} dx_1 + \int_{\frac{\pi}{2} + \frac{\theta}{2} - \frac{\alpha}{2}}^{\frac{5\pi}{2} - \frac{\theta}{2} - \frac{\alpha}{2}} r \sin \frac{\alpha}{2} + r \cos \left(x_1 - \frac{\theta}{2} \right) dx_1 + \int_{\frac{5\pi}{2} - \frac{\theta}{2} - \frac{\alpha}{2}}^{\frac{3\pi}{2}} 2r \sin \frac{\alpha}{2} dx_1 \right) \quad (5.1)$$

$$= \frac{r}{\pi} \left(\theta \sin \frac{\alpha}{2} - \cos \frac{\alpha}{2} + \cos \left(\frac{\alpha}{2} + \theta \right) \right) \quad (5.2)$$

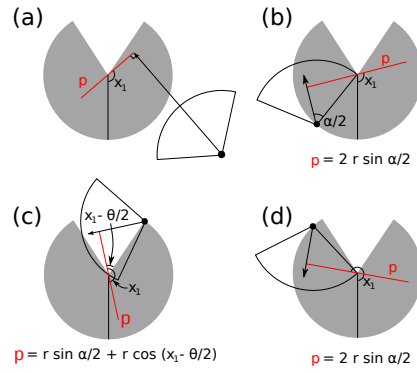


Figure 5.3: An overview of the derivation of the average profile \bar{p} for the gREM submodel SE2, where (a) shows the location of the profile p (the line an animal must pass through in order to be captured) in red and the focal angle, x_1 , for an animal (filled circle), its signal (unfilled sector), and direction of movement (shown as an arrow). The detection zone of the sensor is shown as a filled grey sector with a detection distance of r . The vertical black line within the circle shows the direction the sensor is facing. The derivation of p changes as the animal approaches the sensor from different directions (shown in b-d), where (b) is the derivation of p when x_1 is in the interval $[\frac{\pi}{2}, \frac{\pi}{2} + \frac{\theta}{2} - \frac{\alpha}{2}]$, (c) p when x_1 is in the interval $[\frac{\pi}{2} + \frac{\theta}{2} - \frac{\alpha}{2}, \frac{5\pi}{2} - \frac{\theta}{2} - \frac{\alpha}{2}]$ and (d) p when x_1 is in the interval $[\frac{5\pi}{2} - \frac{\theta}{2} - \frac{\alpha}{2}, \frac{3\pi}{2}]$, where θ , sensor detection width; α , animal signal width. The resultant equation for p is shown beneath b-d. The average profile \bar{p} is the size of the profile averaged across all approach angles.

We then use this expression to calculate density

$$D = z/vt\bar{p}. \quad (5.3)$$

Rather than having one equation that describes \bar{p} globally, the gREM must be split into submodels due to discontinuous changes in p as α and β change. These discontinuities can occur for a number of reasons such as a profile switching between being limited by α and θ , the difference between very small profiles and profiles of size zero, and the fact that the width of a sector stops increasing once the central angle reaches π radians (i.e., a semi-circle is just as wide as a full circle). As an example, if α is small, there is an interval between Figure 5.3c and 5.3d where the ‘blind spot’ would prevent animals being detected giving $p = 0$. This would require an extra integral in our equation, as simply putting our small value of α into 5.1 would not give us this integral of $p = 0$.

gREM submodel specifications were done by hand, and the integration was done using SymPy [51] in Python (Appendix S3). The gREM submodels were checked by confirming that: (1) submodels adjacent in parameter space were equal at the boundary between them; (2) submodels that border $\alpha = 0$ had $p = 0$ when $\alpha = 0$; (3) average profile widths \bar{p} were between 0 and $2r$ and; (4) each integral, divided by the range of angles that it was integrated

over, was between 0 and $2r$. The scripts for these tests are included in Appendix S3 and the R [52] implementation of the gREM is given in Appendix S4.

5.3.2 Simulation Model

We tested the accuracy and precision of the gREM by developing a spatially explicit simulation of the interaction of sensors and animals using different combinations of sensor detection widths, animal signal widths, number of captures, and models of animal movement. One hundred simulations were run where each consisted of a 7.5 km by 7.5 km square with periodic boundaries. A stationary sensor of radius r , 10 m, was set up in the exact centre of each simulated study area, covering seven sensor detection widths θ , between 0 and 2π ($2/9\pi$, $4/9\pi$, $6/9\pi$, $8/9\pi$, $10/9\pi$, $14/9\pi$, and 2π). Each sensor was set to record continuously and to capture animal signals instantaneously from emission. Each simulation was populated with a density of 70 animals km^{-2} , calculated from the equation in [53] as the expected density of mammals weighing 1 g. This density therefore represents a reasonable estimate of density of individuals, given that the smallest mammal is around 2 g [17]. A total of 3937 individuals per simulation were created which were placed randomly at the start of the simulation. 11 signal widths α between 0 and π were used ($1/11\pi$, $2/11\pi$, $3/11\pi$, $4/11\pi$, $5/11\pi$, $6/11\pi$, $7/11\pi$, $8/11\pi$, $9/11\pi$, $10/11\pi$, π).

Each simulation lasted for N steps (14400) of duration T (15 minutes) giving a total duration of 150 days. The individuals moved within each step with a distance d , with an average speed, v . The distance, d , was sampled from a normal distribution with mean distance, $\mu_d = vT$, and standard deviation, $\sigma_d = vT/10$, where the standard deviation was chosen to scale with the average distance travelled. An average speed, $v = 40 \text{ km day}^{-1}$, was chosen based on the largest day range of terrestrial animals [48], and represents the upper limit of realistic speeds. At the end of each step, individuals were allowed to either remain stationary for a time step (with a given probability, S), or change direction where the change in direction has a uniform distribution in the interval $[-A, A]$. This resulted in seven different movement models where: (1) simple movement, where S and $A = 0$; (2) stop-start movement, where (i) $S = 0.25$, $A = 0$, (ii) $S = 0.5$, $A = 0$, (iii) $S = 0.75$, $A = 0$; (3) correlated random walk movement, where (i) $S = 0$, $A = \pi/3$, (ii) $S = 0$, $A = 2\pi/3$, (iii) $S = 0$, $A = \pi$. Individuals were counted as they moved into the detection zone of the sensor per simulation.

We calculated the estimated animal density from the gREM by summing the number of captures per simulation and inputting these values into the correct gREM submodel. The accuracy of the gREM was determined by comparing the true simulation density with the estimated density. Precision of the gREM was determined by the standard deviation of estimated densities.

We used this method to compare the accuracy and precision of all the gREM submodels. As these submodels are derived for different combinations of α and θ , the accuracy and precision of the submodels was used to determine the impact of different values of α and θ .

The influence of the number of captures and animal movement models on accuracy and precision was investigated using four different gREM submodels representative of the range α and θ values (submodels NW1, SW1, NE1, and SE3, Figure 5.2). From a random starting point we ran the simulation until a range of different capture numbers were recorded (from 10 to 100 captures), recorded the length of time this took, and estimated the animal density for each of the four sub-models. These estimated densities were compared to the true density to assess the impact on the accuracy and precision of the gREM. We calculated the coefficient of variation in order to compare the precision of the density estimates from simulations with different expected numbers of captures. The gREM also assumes that individuals move continuously with straight-line movement (simple movement model) and we therefore assessed the impact of breaking the gREM assumptions. We used the four submodels to compare the accuracy and precision of a simple movement model, stop-start movement models (using different average amounts of time spent stationary), and random walk movement models. Finally, as the parameters (α , β , r and v) are likely to be measured with error, we compared true simulation densities to densities estimated with parameters with errors of 0%, $\pm 5\%$ and $\pm 10\%$, for all gREM submodels.

5.4 Results

5.4.1 Analytical model

The equation for \bar{p} has been newly derived for each submodel in the gREM, except for the gas model and REM which have been calculated previously. However, many models, although derived separately, have the same expression for \bar{p} . Figure 5.4 shows the expression for \bar{p} in each case. The general equation for density, 5.3, is used with the correct value of \bar{p} substituted. Although more thorough checks are performed in Appendix S3, it can be seen that all adjacent expressions in Figure 5.4 are equal when expressions for the boundaries between them are substituted in.

5.4.2 Simulation model

5.4.2.1 gREM submodels

All gREM submodels showed a high accuracy, i.e., the median difference between the estimated and true values was less than 2% across all models (Figure 5.5). However, the precision of the submodels do vary, where the gas model is the most precise and the SW7 sub model the least precise, having the smallest and the largest interquartile range, respectively (Figure 5.5). The

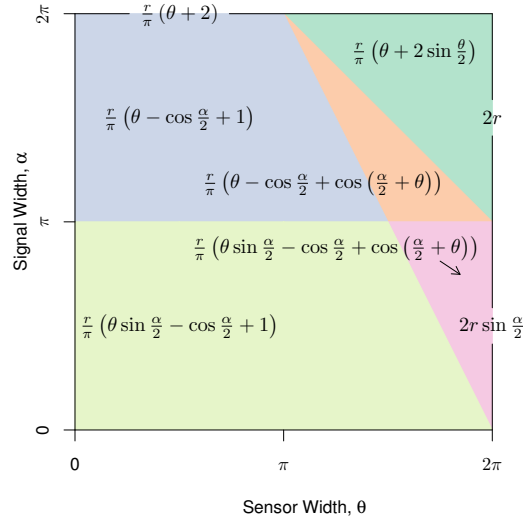


Figure 5.4: Expressions for the average profile width, \bar{p} , given a range of sensor and signal widths. Despite independent derivation within each block, many models result in the same expression. These are collected together and presented as one block of colour. Expressions on the edge of the plot are for submodels with $\alpha, \theta = 2\pi$.

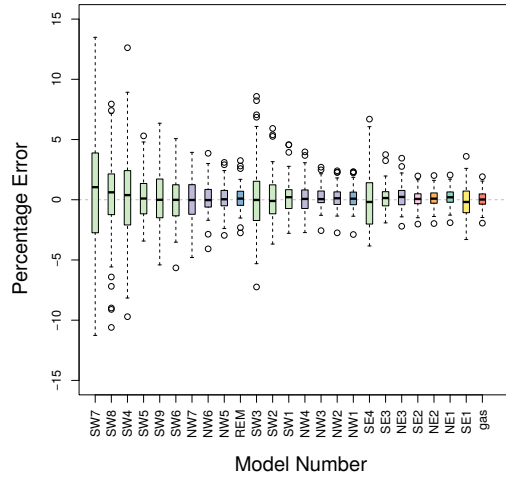


Figure 5.5: Simulation model results of the accuracy and precision for gREM submodels. The percentage error between estimated and true density for each gREM sub model is shown within each box plot, where the black line represents the median percentage error across all simulations, boxes represent the middle 50% of the data, whiskers represent variability outside the upper and lower quartiles with outliers plotted as individual points. Box colours correspond to the expressions for average profile width \bar{p} given in Figure 4.

standard deviation of the error between the estimated and true densities is strongly related to both the sensor and signal widths (Appendix S5), such that larger widths have lower standard deviations (greater precision) due to the increased capture rate of these models.

5.4.2.2 Number of captures

Within the four gREM submodels tested (NW1, SW1, SE3, NE1), the accuracy was not strongly affected by the number of captures. The median difference between the estimated and true

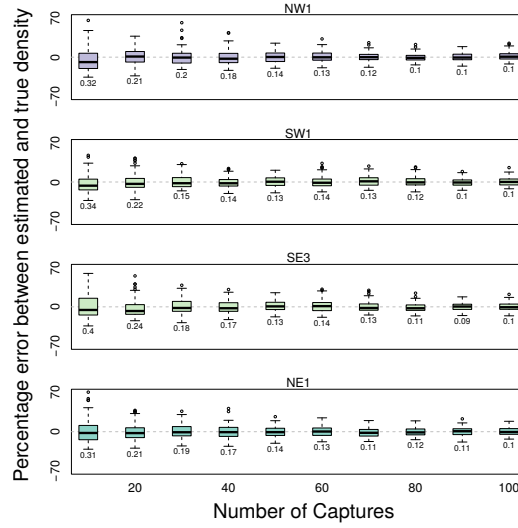


Figure 5.6: Simulation model results of the accuracy and precision of four gREM submodels (NW1, SW1, SE3 and NE1) given different numbers of captures. The percentage error between estimated and true density within each gREM sub model for capture rate is shown within each box plot, where the black line represents the median percentage error across all simulations, boxes represent the middle 50% of the data, whiskers represent variability outside the upper and lower quartiles with outliers plotted as individual points. Sensor and signal widths vary between submodels. The numbers beneath each plot represent the coefficient of variation. The colour of each box plot corresponds to the expressions for average profile width \bar{p} given in Figure 4.

values was less than 15% across all capture rates (Figure 5.6). However, the precision was dependent on the number of captures across all four of the gREM submodels, where precision increases as number of captures increases, as would be expected for any statistical estimate (Figure 5.6). For all gREM submodels, the the coefficient of variation falls to 10% at 100 captures.

5.4.2.3 Movement models

Within the four gREM submodels tested (NW1, SW1, SE3, NE1), neither the accuracy or precision was affected by the average amount of time spent stationary. The median difference between the estimated and true values was less than 2% for each category of stationary time (0, 0.25, 0.5 and 0.75) (Figure 5.7a). Altering the maximum change in direction in each step (0, $\pi/3$, $2\pi/3$, and π) did not affect the accuracy or precision of the four gREM submodels (Figure 5.7b).

5.4.2.4 Impact of parameter error

The percentage error in the density estimates across all parameters and gREM submodels shows a similar response for under and over estimated parameters, suggesting the accuracy is reasonable with respect to parameter error (Appendix S6). The impact of parameter error on the precision of the density estimate varies across gREM submodels and parameters, where α shows the

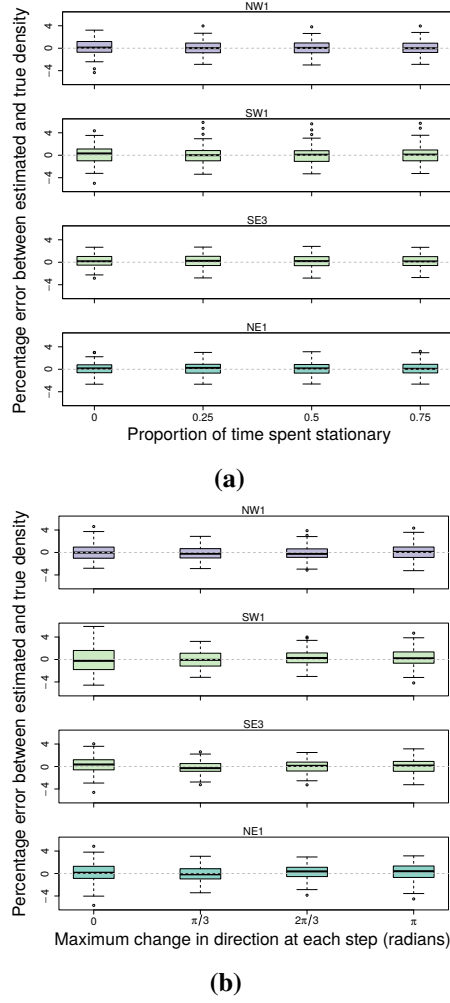


Figure 5.7: Simulation model results of the accuracy and precision of four gREM submodels (NW1, SW1, SE3 and NE1) given different movement models where (a) average amount of time spent stationary (stop-start movement) and (b) maximum change in direction at each step (correlated random walk model). The percentage error between estimated and true density within each gREM sub model for the different movement models is shown within each box plot, where the black line represents the median percentage error across all simulations, boxes represent the middle 50% of the data, whiskers represent variability outside the upper and lower quartiles with outliers plotted as individual points. The simple model is represented where time and maximum change in direction equals 0. The colour of each box plot corresponds to the expressions for average profile width \bar{p} given in Figure 4.

largest variation including the largest values. However, in all cases the percentage error in the density estimate is not more than 5% greater than the error in the parameter estimate (Appendix S6).

5.5 Discussion

5.5.1 Analytical model

We have developed the gREM such that it can be used to estimate density from acoustic sensors and camera traps. This has entailed a generalisation of the gas model and the REM in [35] to be

applicable to any combination of sensor width θ and signal directionality α . We emphasise that the approach is robust to multiple detections of the same individual. We have used simulations to show, as a proof of principle, that these models are accurate and precise.

There are a number of possible extensions to the gREM which could be developed in the future. The original gas model was formulated for the case where both animals and sensor are moving [46]. Indeed any of the models which have animals that are equally detectable in all directions ($\alpha = 2\pi$) can be trivially expanded by replacing animal speed v with $v + v_s$ where v_s is the speed of the sensor. However, when the animal has a directional call the extension becomes less simple. The approach would be to calculate again the mean profile width. However, for each angle of approach, one would have to average the profile width for an animal facing in any direction (i.e., not necessarily moving towards the sensor) weighted by the relative velocity of that direction. There are a number of situations where a moving detector and animal could occur, e.g. an acoustic detector towed from a boat when studying porpoises [54] or surveying echolocating bats from a moving car [55].

Interesting but unstudied problems impacting the gREM are firstly, edge effects caused by sensor trigger delays (the delay between sensing an animal and attempting to record the encounter) [56], and secondly, sensors which repeatedly turn on and off during sampling [55]. The second problem is particularly relevant to acoustic detectors which record ultrasound by time expansion. Here ultrasound is recorded for a set time period and then slowed down and played back, rendering the sensor 'deaf' periodically during sampling. Both of these problems may cause biases in the gREM, as animals can move through the detection zone without being detected. As the gREM assumes constant surveillance, the error created by switching the sensor on and off quickly will become more important if the sensor is only on for short periods of time. We recommend that the gREM is applied to constantly sampled data, and the impacts of breaking these assumptions on the gREM should be further explored.

5.5.2 Accuracy, Precision and Recommendations for Best Practice

Based on our simulations, we believe that the gREM has the potential to produce accurate estimates for many different species, using either camera traps or acoustic detectors. However, the precision of the gREM differed between submodels. For example, when the sensor and signal width were small, the precision of the model was reduced. Therefore when choosing a sensor for use in a gREM study, the sensor detection width should be maximised. If the study species has a narrow signal directionality, other aspects of the study protocol, such as length of the survey, should be used to compensate.

The precision of the gREM is greatly affected by the number of captures. The coefficient

of variation falls dramatically between 10 and 60 captures and then after this continues to slowly reduce. At 100 captures the submodels reach 10% coefficient of variation, considered to be a very good level of precision and better than many previous studies [57, 58, 59]. The length of surveys in the field will need to be adjusted so that enough data can be collected to reach this precision level. Populations of fast moving animals or populations with high densities will require less survey effort than those species that are slow moving or have populations with low densities.

We found that the sensitivity of the gREM to inaccurate parameter estimates was both predictable and reasonable (Appendix S6), although this varies between different parameters and gREM submodels. Whilst care should be taken in parameter estimation when analysing both acoustic and camera trap data, acoustic data poses particular problems. For acoustic surveys, estimates of r (detection distance) can be measured directly or calculated using sound attenuation models [49], while the sensor angle is often easily measured [50] or found in the manufacturer's specifications. When estimating animal movement speed v , only the speed of movement during the survey period should be used. The signal width is the most sensitive parameter to inaccurate estimates (Appendix S6) and is also the most difficult to measure. While this parameter will typically be assumed to be 2π for camera trap surveys, fewer estimates exist for acoustic signal widths. Although signal width has been measured for echolocating bats using arrays of microphones [47], more work should be done on obtaining estimates for a range of acoustically surveyed species.

5.5.3 Limitations

Although the REM has been found to be effective in field tests [35, 34], the gREM requires further validation by both field tests and simulations. For example, capture-mark-recapture methods could be used alongside the gREM to test the accuracy under field conditions [35]. While we found no effect of the movement model on the accuracy or precision of the gREM, the models we have used in our simulations to validate the gREM are still simple representations of true animal movement. Animal movement may be highly nonlinear and often dependent on multiple factors such as behavioural state and existence of home ranges [60]. Therefore testing the gREM against real animal data, or further simulations with more complex movement models, would be beneficial.

The assumptions of our simulations may require further consideration, for example we have assumed an equal density across the study area. However, in a field environment the situation may be more complex, with additional variation coming from local changes in density between sensor sites. Although unequal densities should theoretically not affect accuracy [46], it

will affect precision and further simulations should be used to quantify this effect. Additionally, we allowed the sensor to be stationary and continuously detecting, negating the triggering, and non-continuous recording issues that could exist with some sensors and reduce precision or accuracy. Finally, in the simulation animals moved at the equivalent of the largest day range of terrestrial animals [48]. Slower speed values should not alter the accuracy of the gREM, but precision would be affected since slower speeds produce fewer records. The gREM was both accurate and precise for all the movement models we tested (stop-start movement and correlated random walks).

A feature of the gREM is that it does not fit a statistical model to estimate detection probability as occupancy models and distance sampling do [32, 30, 31]. Instead it explicitly models the process, with animals only being detected if they approach the sensor from a suitable direction. Other processes that affect detection probability could be included in the model to improve realism.

5.5.4 Implications for ecology and conservation

The gREM is applicable for count data obtained either visually or acoustically in both marine and terrestrial environments, and is suitable for taxa including echolocating bats [24], songbirds [61], whales [31] and forest primates [62]. Many of these taxa contain critically endangered species and monitoring their populations is of conservation interest. For example, current methods of density estimation for the threatened Franciscana dolphin (*Pontoporia blainvillei*) may result in underestimation of their numbers [63]. In addition, using gREM may be easier than other methods for measuring the density of animals which may be useful in quantifying ecosystem services, such as songbirds with a known positive influence on pest control [64].

The gREM will aid researchers to study species with non-invasive methods such as remote sensors, which allows for large, continuous monitoring projects with limited human resources [65]. The gREM is also suitable for species that are sensitive to human contact or are difficult or dangerous to catch [57]. As sensors such as camera traps and acoustic detectors become more ubiquitous, the gREM will be increasingly useful for monitoring unmarked animal populations across broad spatial, temporal and taxonomic scales.

5.6 Acknowledgments

We thank Hilde Wilkinson-Herbot, Chris Carbone, Francois Balloux, Andrew Cunningham, Steve Hailes, Richard Glennie and an anonymous referee for comments on previous versions of the manuscript. This study was funded through CoMPLEX PhD studentships at University College London supported by BBSRC and EPSRC (EAM and TCDL) and The Darwin Initia-

tive (Awards 15003, 161333, EIDPR075), NERC (NE/H525003/1), and The Leverhulme Trust (Philip Leverhulme Prize) for KEJ.

5.7 Data Accessibility

The code used in this paper is available on Github at <https://github.com/timcdlucas/lucasMoorcroftManuscript/tree/postPeerReview>.

Chapter 6

General Conclusions

Lorem ipsum dolor sit amet, consectetur adipiscing elit. Etiam lobortis facilisis sem. Nullam nec mi et neque pharetra sollicitudin. Praesent imperdiet mi nec ante. Donec ullamcorper, felis non sodales commodo, lectus velit ultrices augue, a dignissim nibh lectus placerat pede. Vivamus nunc nunc, molestie ut, ultricies vel, semper in, velit. Ut porttitor. Praesent in sapien. Lorem ipsum dolor sit amet, consectetur adipiscing elit. Duis fringilla tristique neque. Sed interdum libero ut metus. Pellentesque placerat. Nam rutrum augue a leo. Morbi sed elit sit amet ante lobortis sollicitudin. Praesent blandit blandit mauris. Praesent lectus tellus, aliquet aliquam, luctus a, egestas a, turpis. Mauris lacinia lorem sit amet ipsum. Nunc quis urna dictum turpis accumsan semper.

Appendix A

gREM Appendix

A.1 Table of symbols

Symbol	Description	Units
θ	Sensor width	rad
α	Animal signal width	rad
x_i	Focal angle, $i \in \{1, 2, 3, 4\}$	rad
r	Detection distance	m
\bar{p}	Average profile width	m
p	A specific profile width	m
v	Velocity	m s^{-1}
t	Time	s
z	Number of detections	-
D	Animal density	m^{-2}
T	Step length	s
N	Number of steps per simulation	-
d	Distance moved in a time step	m
S	Probability of remaining stationary	-
A	Maximum turning angle	rad

Table A.1: List of symbols used to describe the *gREM* and simulations. ‘-’ means the quantity has no units.

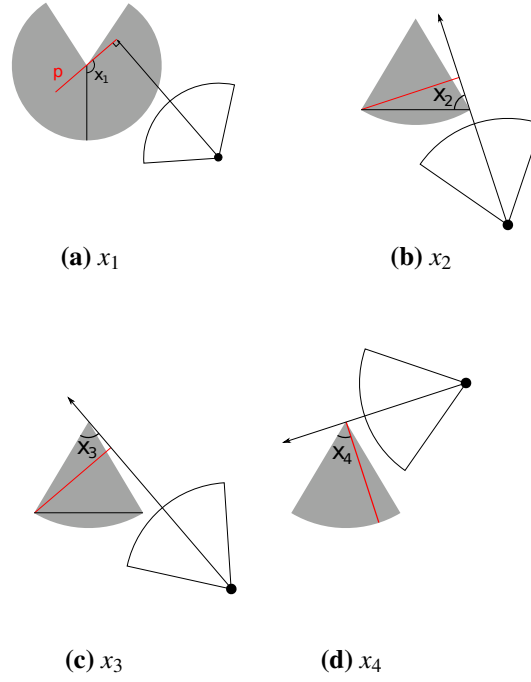


Figure A.1: The location of the focal angles $x_{i \in [1,4]}$. x_1 is used in SE and NE models (including the gas model). $x_2 - x_4$ are used in NW and SW models. The sector shaped detection region is shown in grey. Animals are filled black circles and the animal signal is an unfilled sector. The animal's direction of movement is indicated with an arrow. The profile p is shown with a red line. (a) Animal is directly approaching the sensor at $x_1 = \frac{\pi}{2}$. (b) Animal is directly approaching the sensor at $x_2 = \frac{\pi}{2}$. x_2 then decreases until the profile is perpendicular to the edge of the detection region. (c) When the profile is perpendicular to the edge of the detection region, $x_3 = \theta$. (d) x_4 measures the angle between the left side of the detection region and the profile.

A.2 Supplementary Methods

A.2.1 Introduction

These supplementary methods derive all the models used. For continuity, the gas model derivation is included here as well as in the main text. The calculation of all integrals use in the gREM is included in the Python script S3.

A.2.2 Gas model

Following [45], we derive the gas model where sensors can capture animals in any direction and animal signals are detectable from any direction ($\theta = 2\pi$ and $\alpha = 2\pi$). We assume that animals are in a homogeneous environment, and move in straight lines of random direction with velocity v . We allow that our stationary sensor can capture animals at a detection distance r and that if an animal moves within this detection zone they are captured with a probability of one, while animals outside the zone are never captured.

In order to derive animal density, we need to consider relative velocity from the reference frame of the animals. Conceptually, this requires us to imagine that all animals are stationary and randomly distributed in space, while the sensor moves with velocity v . If we calculate the area covered by the sensor during the survey period we can estimate the number of animals the sensor should capture. As a circle moving across a plane, the area covered by the sensor per unit time is $2rv$. The number of expected captures, z , for a survey period of t , with an animal density of D is $z = 2rvtD$. To estimate the density, we rearrange to get $D = z/2rvt$.

A.2.2.1 gREM derivations for different detection and signal widths

Different combinations of θ and α would be expected to occur (e.g., sensors have different detection widths and animals have different signal widths). For different combinations θ and α , the area covered per unit time is no longer given by $2rv$. Instead of the size of the sensor detection zone having a diameter of $2r$, the size changes with the approach angle between the sensor and the animal. For any given signal width and detector width and depending on the angle that the animal approaches the sensor, the width of the area within which an animal can be detected is called the profile, p . The size of the profile (averaged across all approach angles) is defined as the average profile \bar{p} . However, different combinations of θ and α need different equations to calculate \bar{p} . This \bar{p} is the only thing that changes

We have identified the parameter space for the combinations of θ and α for which the derivation of the equations are the same (defined as sub-models in the gREM) (Fig. 5.2). For example, the gas model becomes the simplest gREM sub-model (upper right in Fig. 5.2) and the REM from [35] is another gREM sub-model where $\theta < \pi/2$ and $\alpha = 2\pi$.

Models with $\theta = 2\pi$ are described first (the gas model described above and SE1). Then models with $\theta > \pi$ are described (NE then SE). Finally models with $\theta < \pi$ (NW then SW) are described.

A.2.3 Model SE1

SE1 is very similar to the gas model except that because $\alpha \leq \pi$ the profile width is no longer $2r$ but is instead limited by the width of the animal signal. We therefore get a profile width of $2r \sin(\alpha/2)$ instead.

$$\bar{p}_{\text{SE1}} = \frac{1}{\pi} \int_{\frac{\pi}{2}}^{\frac{3\pi}{2}} 2r \sin\left(\frac{\alpha}{2}\right) dx_1 \quad (\text{A.1})$$

$$\bar{p}_{\text{SE1}} = 2r \sin\left(\frac{\alpha}{2}\right) \quad (\text{A.2})$$

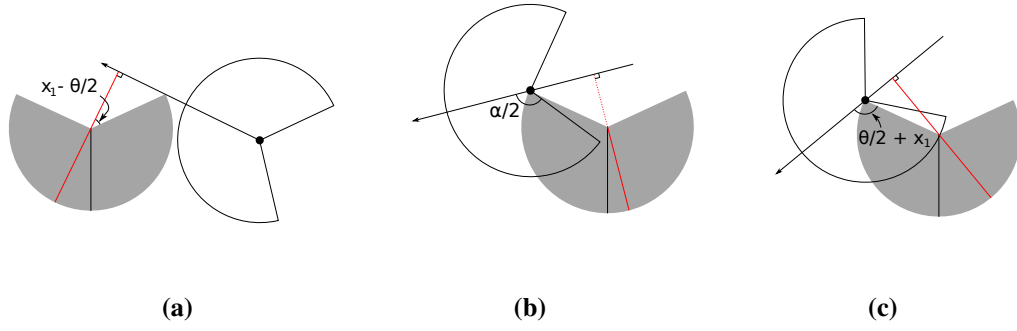


Figure A.2: Three of the integrals in NE models. The sector shaped detection region is shown in grey. Animals are filled black circles and the animal signal is an unfilled sector. The animals direction of movement is indicated with an arrow. The profile p is shown with a red line. Dashed red lines indicate areas where animals cannot be detected. (a) The second integral in NE with width $r + r \cos(x_1 - \theta/2)$ (b) The third integral in NE3. $\alpha/2$ is labelled. As it is small, animals to the right of the detector cannot be detected. (c) After further rotation, $\alpha/2$ is now bigger than the angle shown and animals to the right of the detector can again be detected.

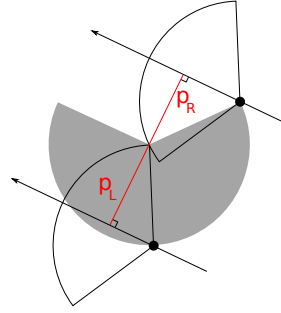


Figure A.3: The second integral in SE. The right side of the profile (p_R) is limited by the size of the sensor region while the left side of the profile (p_L) is limited by the size of the signal width. The full profile has width $p = r \sin(\alpha/2) + r \cos(\theta/2 - x_1)$. The sector shaped detection region is shown in grey. Animals are filled black circles and the animal signal is an unfilled sector. The animals direction of movement is indicated with an arrow. The profile p is shown with a red line.

This profile is integrated over the interval $[\frac{\pi}{2}, \frac{3\pi}{2}]$ which is π radians of rotation starting with the animal moving directly towards the sensor (Fig. A.1a).

A.2.4 Models NE1–3

When the detection zone is not a circle, we have more complex profiles and need to explicitly write functions for the width of the profile for every approach angle. We then use these functions to find the average profile width \bar{p} for all approach angles by integrating across all 2π angles of approach and dividing by 2π .

There are three submodels within quadrant NE (Fig. 5.2). Note that NE1 covers the area $\alpha = 2\pi$ as well as the triangle below it as these two models are specified exactly the same, rather than happening to have equal results.

These models have up to five profiles.

1. The profile width starts, from $x_1 = \frac{\pi}{2}$ as $2r$.
2. At $x_1 = \theta/2$, the right hand side of the profile cannot be r wide as the corner of the ‘blind spot’ limits its size to being $r \cos(x_1 - \theta/2)$ wide (Fig. A.2a).
3. The third profile is only found in NE3. If $\alpha < 4\pi - 2\theta$, then at $x_1 = \theta/2 + \pi/2$, when the profile is perpendicular to the edge of the blind spot, the whole right side of the profile is invisible to the sensor (Fig. A.2b). This gives a profile size of just r .
4. At some point, the sensor can detect animals once they have passed the blind spot giving a profile width of $r + r \cos(x_1 + \theta/2)$ (Fig. A.2c). From $x_1 = \pi$, if the animal signal is wide enough to be detected in this area, this is the wider profile. This then defines the split between NE1 and NE2. In NE1, with $\alpha > 3\pi - \theta$, the animal signal is wide enough that at $x_1 = \pi$ the animal can immediately be detected past the blind spot and so this profile is used. In NE2, with $\alpha < 3\pi - \theta$, the latter profile is reached at $5\pi/2 - \theta/2 - \alpha/2$.
5. Finally, common to all three models, at $x_1 = 2\pi - \theta/2$ the profile becomes a full $2r$ once again.

A.2.4.1 Model NE1

Submodel NE1 exists within the area bounded by $\alpha \leq 2\pi$, $\theta \leq 2\pi$ and $\alpha \geq 3\pi - \theta$ (Fig. 5.2). It has four profiles; it does not include the r profile at $x_1 = \pi$ (profile described in point (3) in Section A.2.4). Furthermore, θ is wide enough that the $r + r \cos(x_1 + \theta/2)$ profile starts at π . This then gives us

$$\bar{p}_{\text{NE1}} = \frac{1}{\pi} \left(\int_{\frac{\pi}{2}}^{\frac{\theta}{2}} 2r \, dx_1 + \int_{\frac{\theta}{2}}^{\pi} r \cos\left(\frac{\theta}{2} - x_1\right) + r \, dx_1 + \int_{\pi}^{2\pi - \frac{\theta}{2}} r \cos\left(\frac{\theta}{2} + x_1\right) + r \, dx_1 + \int_{2\pi - \frac{\theta}{2}}^{\frac{3\pi}{2}} 2r \, dx_1 \right) \quad (\text{A.3})$$

$$\bar{p}_{\text{NE1}} = \frac{r}{\pi} \left(\theta + 2 \sin\left(\frac{\theta}{2}\right) \right) \quad (\text{A.4})$$

A.2.4.2 Model NE2

Model NE2 is bounded by $\alpha \leq 3\pi - \theta$, $\alpha \geq 4\pi - 2\theta$ and $\alpha \geq \pi$ (Fig. 5.2). It is the same as NE1 except that the third profile starts at $5\pi/2 - \theta/2 - \alpha/2$ instead of at π which is reflected

in the different bounds in the second and third integral.

$$\bar{p}_{\text{NE2}} = \frac{1}{\pi} \left(\int_{\frac{\pi}{2}}^{\frac{\theta}{2}} 2r \, dx_1 + \int_{\frac{\theta}{2}}^{\frac{5\pi}{2} - \frac{\theta}{2} - \frac{\alpha}{2}} r \cos\left(\frac{\theta}{2} - x_1\right) + r \, dx_1 + \int_{\frac{5\pi}{2} - \frac{\theta}{2} - \frac{\alpha}{2}}^{2\pi - \frac{\theta}{2}} r \cos\left(\frac{\theta}{2} + x_1\right) + r \, dx_1 + \int_{2\pi - \frac{\theta}{2}}^{\frac{3\pi}{2}} 2r \, dx_1 \right) \quad (\text{A.5})$$

$$\bar{p}_{\text{NE2}} = \frac{r}{\pi} \left(\theta - \cos\left(\frac{\alpha}{2}\right) + \cos\left(\frac{\alpha}{2} + \theta\right) \right) \quad (\text{A.6})$$

A.2.4.3 Model NE3

Model NE3 is bound by $\alpha \leq 4\pi - 2\theta$, $\alpha \geq \pi$ and $\theta \geq \pi$ (Fig. 5.2). It is the same as NE2 except that it contains the extra profile with width r (third integral).

$$\bar{p}_{\text{NE3}} = \frac{1}{\pi} \left(\int_{\frac{\pi}{2}}^{\frac{\theta}{2}} 2r \, dx_1 + \int_{\frac{\theta}{2}}^{\frac{\theta}{2} + \frac{\pi}{2}} r \cos\left(\frac{\theta}{2} - x_1\right) + r \, dx_1 + \int_{\frac{\theta}{2} + \frac{\pi}{2}}^{\frac{5\pi}{2} - \frac{\theta}{2} - \frac{\alpha}{2}} r \, dx_1 + \int_{\frac{5\pi}{2} - \frac{\theta}{2} - \frac{\alpha}{2}}^{2\pi - \frac{\theta}{2}} r \cos\left(\frac{\theta}{2} + x_1\right) + r \, dx_1 + \int_{2\pi - \frac{\theta}{2}}^{\frac{3\pi}{2}} 2r \, dx_1 \right) \quad (\text{A.7})$$

$$\bar{p}_{\text{NE3}} = \frac{r}{\pi} \left(\theta - \cos\left(\frac{\alpha}{2}\right) + 1 \right) \quad (\text{A.8})$$

A.2.5 Models SE2–4

Quadrant SE contains three submodels excluding SE1 (Fig. 5.2). The differences between these three models are similar to the differences between the models in NE. There are four possible profiles.

1. As α is less than π the profile is smaller than $2r$, even when the sensor width is a full diameter. The profile width starts as $2r \sin(\alpha/2)$.
2. Similar to NE, at a certain point the blind spot of the sensor area limits the profile width on one side. This gives a profile width of $r \sin(\alpha/2) + r \cos(x_1 - \theta/2)$ (Fig. A.3).
3. Also similar to NE, there can be a point where the right side of the profile is 0 giving a profile width of $r \sin(\alpha/2)$.
4. If $\alpha \leq 2\pi - \theta$, then at $x_1 = \theta/2 + \pi/2 + \alpha/2$ the profile width becomes 0. This inequality distinguishes between SE3 and SE4.

5. The third profile $r \sin(\alpha/2)$ starts at $\theta/2 + \pi/2$ while at $5\pi/2 - \alpha/2 - \theta/2$ the profile returns to size $2r \sin(\alpha/2)$. If $\theta/2 + \pi/2 \geq 5\pi/2 - \alpha/2 - \theta/2$ we go straight into the $2r \sin(\alpha/2)$ profile and miss the $r \sin(\alpha/2)$ profile. SE2 and SE3 are separated by this inequality which simplifies to $\alpha \leq 4\pi - 2\theta$.

A.2.5.1 Model SE2

SE2 is bounded by $\alpha \geq 4\pi - 2\theta$, $\alpha \leq \pi$ and $\theta \leq 2\pi$ (Fig. 5.2). As $\alpha \geq 4\pi - 2\theta$, there is no $r \sin(\alpha/2)$ profile. As $\alpha \leq 4\pi - 2\theta$, the profile returns to $2r \sin(\alpha/2)$ rather than going to 0. These integrals relate to profiles (1), (2) and (5) in Section A.2.5.

$$\bar{p}_{\text{SE2}} = \frac{1}{\pi} \left(\int_{\frac{\pi}{2}}^{\frac{\pi}{2} + \frac{\theta}{2} - \frac{\alpha}{2}} 2r \sin\left(\frac{\alpha}{2}\right) dx_1 + \int_{\frac{\pi}{2} + \frac{\theta}{2} - \frac{\alpha}{2}}^{\frac{5\pi}{2} - \frac{\theta}{2} - \frac{\alpha}{2}} r \sin\left(\frac{\alpha}{2}\right) + r \cos\left(\frac{\theta}{2} - x_1\right) dx_1 + \int_{\frac{5\pi}{2} - \frac{\theta}{2} - \frac{\alpha}{2}}^{\frac{3\pi}{2}} 2r \sin\left(\frac{\alpha}{2}\right) dx_1 \right) \quad (\text{A.9})$$

$$\bar{p}_{\text{SE2}} = \frac{r}{\pi} \left(\theta \sin\left(\frac{\alpha}{2}\right) - \cos\left(\frac{\alpha}{2}\right) + \cos\left(\frac{\alpha}{2} + \theta\right) \right) \quad (\text{A.10})$$

A.2.5.2 Model SE3

SE3 is bounded by $4\pi - 2\theta \leq \alpha \leq 4\pi - 2\theta$ and $\alpha \leq \pi$ (Fig. 5.2). Therefore there is a $r \sin(\alpha/2)$ profile but no $0r$ profile. This relates to profiles (1), (2), (3) and (5) above.

$$\bar{p}_{\text{SE3}} = \frac{1}{\pi} \left(\int_{\frac{\pi}{2}}^{\frac{\pi}{2} + \frac{\theta}{2} - \frac{\alpha}{2}} 2r \sin\left(\frac{\alpha}{2}\right) dx_1 + \int_{\frac{\pi}{2} + \frac{\theta}{2} - \frac{\alpha}{2}}^{\frac{\theta}{2} + \frac{\pi}{2}} r \sin\left(\frac{\alpha}{2}\right) + r \cos\left(\frac{\theta}{2} - x_1\right) dx_1 + \int_{\frac{\theta}{2} + \frac{\pi}{2}}^{\frac{5\pi}{2} - \frac{\theta}{2} - \frac{\alpha}{2}} r \sin\left(\frac{\alpha}{2}\right) dx_1 + \int_{\frac{5\pi}{2} - \frac{\theta}{2} - \frac{\alpha}{2}}^{\frac{3\pi}{2}} 2r \sin\left(\frac{\alpha}{2}\right) dx_1 \right) \quad (\text{A.11})$$

$$\bar{p}_{\text{SE3}} = \frac{r}{\pi} \left(\theta \sin\left(\frac{\alpha}{2}\right) - \cos\left(\frac{\alpha}{2}\right) + 1 \right) \quad (\text{A.12})$$

A.2.5.3 Model SE4

Finally SE4 is bounded by $\alpha \leq 4\pi - 2\theta$, $\alpha \leq \pi$ and $\theta \leq \pi$ (Fig. 5.2). It is the same as SE3 except that the profile becomes 0 rather than returning to $2r \sin(\alpha/2)$. This relates to profiles (1), (2), (3) and (4) above though profile (4) with width 0 is not shown.

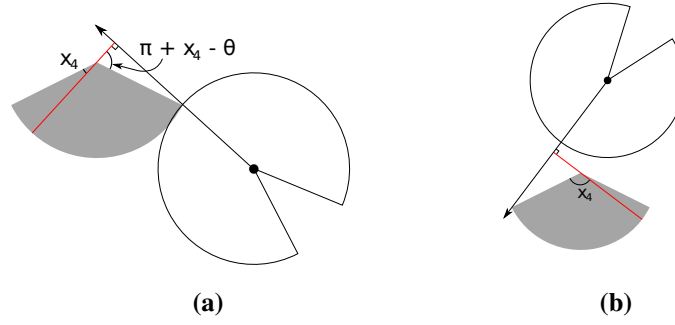


Figure A.4: The second and fourth profiles of NW1. The left side of both profiles is of width r while the right side differs. (a) The right side of the profile is $r \cos(\pi + x_4 - \theta) = -r \cos(\theta - x_4)$ (b) The right side is $r \cos(\pi - x_4) = -r \cos x_4$ respectively. In both images the sector shaped detection region is shown in grey. Animals are filled black circles and the animal signal is an unfilled sector. The animals direction of movement is indicated with an arrow. The profile p is shown with a red line.

$$\bar{p}_{SE4} = \frac{1}{\pi} \left(\int_{\frac{\pi}{2}}^{\frac{\pi}{2} + \frac{\theta}{2} - \frac{\alpha}{2}} 2r \sin\left(\frac{\alpha}{2}\right) dx_1 + \int_{\frac{\pi}{2} + \frac{\theta}{2} - \frac{\alpha}{2}}^{\frac{\theta}{2} + \frac{\pi}{2}} r \sin\left(\frac{\alpha}{2}\right) + r \cos\left(\frac{\theta}{2} - x_1\right) dx_1 + \int_{\frac{\theta}{2} + \frac{\pi}{2}}^{\frac{\alpha}{2} + \frac{\theta}{2} + \frac{\pi}{2}} r \sin\left(\frac{\alpha}{2}\right) dx_1 \right) \quad (\text{A.13})$$

$$\bar{p}_{SE4} = \frac{r}{\pi} \left(\theta \sin\left(\frac{\alpha}{2}\right) - \cos\left(\frac{\alpha}{2}\right) + 1 \right) \quad (\text{A.14})$$

A.2.6 Model NW1

NW1 is the first model with $\theta < \pi$. Whereas previously the focal angle has always been x_1 , we now use different focal angles. x_2 and x_3 correspond to γ_1 and γ_2 in [35] while x_4 is new. They are described in Fig. A.1b–d.

There are five different profiles in NW1.

1. x_2 has an interval of $[\pi/2, \theta/2]$ which is from the angle of approach being directly towards the sensor until the profile is parallel to the left hand radius of the sensor sector (Fig. A.1b). During this interval the profile width is $2r \sin(\theta/2) \sin(x_2)$ which is calculated using the equation for the length of a chord. Note that while rotating anti-clockwise (as usual) x_2 decreases in size.
2. From here, we examine focal angle x_4 (note that x_3 is used in later models, but is not relevant here.) The left side of the profile is a full radius while the right side is limited to $-r \cos(x_4 - \theta)$ (Fig. A.4a).

3. At $x_4 = \theta - \pi/2$, the profile is perpendicular to the edge of the sensor area. Here, the right side of the profile is $0r$ giving a profile size of r .
4. When $x_4 = \pi/2$ the angle of approach is from behind the sensor, but we can once again be detected on the right side of the sensor (Fig. A.4b). Therefore the width of the profile is $r - r \cos(x_4)$.
5. Finally, we have the x_2 profile, but from behind.

$$\bar{p}_{NW1} = \frac{1}{\pi} \left(\int_{\frac{\theta}{2}}^{\frac{\pi}{2}} 2r \sin\left(\frac{\theta}{2}\right) \sin(x_2) dx_2 + \int_0^{\theta - \frac{\pi}{2}} r - r \cos(-x_4 + \theta) dx_4 \right. \\ \left. + \int_{\theta - \frac{\pi}{2}}^{\frac{\pi}{2}} r dx_4 + \int_{\frac{\pi}{2}}^{\theta} r - r \cos(x_4) dx_4 + \int_{\frac{\theta}{2}}^{\frac{\pi}{2}} 2r \sin\left(\frac{\theta}{2}\right) \sin(x_2) dx_2 \right) \quad (A.15)$$

$$\bar{p}_{NW1} = \frac{r}{\pi} (\theta + 2) \quad (A.16)$$

A.2.7 Models NW2–4

The models NW2–4 have the five potential profiles in NW1 but not all profiles occur in each model, and the angle at which transitions occur are different. Furthermore, there is one extra profile possible.

1. When approaching the sensor from behind, there is a period where the profile is r wide as in NW1 profile (3).
2. At some point after profile (1) animals to the right of the sensor can be detected again. If this occurs in the x_4 region, the profile width becomes $r - r \cos(x_4)$ as in NW1.
3. However, as α is now less than 2π , animals to the right of the sensor may be undetectable until we are in the second x_2 region. In this case, when we first enter the second x_2 region, the profile has a width of $r \cos(x_2 - \theta/2)$. This occurs only if $\alpha \leq 3\pi - 2\theta$. This inequality is found by noting that animals to the right of the sensor can be detected again at $x_4 = 3\pi/2 - \alpha$ but the x_2 region starts at $x_4 = \theta$. The new profile in x_2 will only occur if $\theta < 3\pi/2 - \alpha/2$ which is rearranged to find the inequality above. This defines the boundary between NW2 and NW3.
4. As $\alpha \leq 2\pi$ it is possible that when the angle of approach is from directly behind the sensor the animal will not be detected at all. This is the case if $\alpha/2 \leq \pi - \theta/2$ (Fig. A.5).

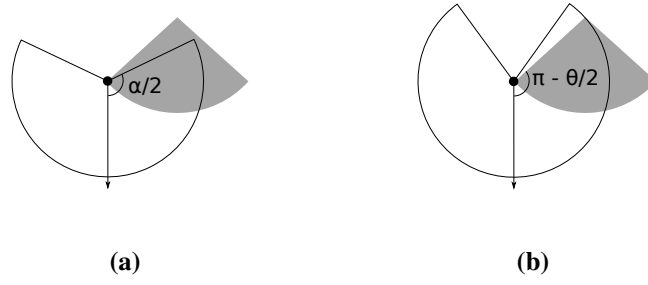


Figure A.5: Profile sizes when an animal approaches from behind in models NW2–4. If α is relatively large, animals can be detected when approaching from behind. Otherwise animals cannot be detected. The sector shaped detection region is shown in grey. Animals are filled black circles and the animal signal is an unfilled sector. The animals direction of movement is indicated with an arrow. (a) If $\alpha/2$ is less than $\pi - \theta/2$, as is the case here, then the width of the profile when an animal approaches directly from behind is zero. (b) If $\alpha/2 > \pi - \theta/2$ the profile width from behind is $2r \sin(\theta/2) \sin(x_2)$.

This inequality (simplified as $\alpha \leq 2\pi - \theta$) defines the boundary between NW3 and NW4.

A.2.7.1 Model NW2

NW2 is bounded by $\alpha \geq 3\pi - 2\theta$, $\alpha \leq 2\pi$ and $\theta \leq \pi$ (Fig. 5.2).

NW2 has all five profiles as found in NW1. However, the change from the r profile (third integral) to the $r - r \cos(x_4)$ profile (fourth integral) occurs at $x_4 = 3\pi/2 - \alpha/2$ instead of at $x_4 = \theta$.

$$\bar{p}_{\text{NW2}} = \frac{1}{\pi} \left(\int_{\frac{\theta}{2}}^{\frac{\pi}{2}} 2r \sin\left(\frac{\theta}{2}\right) \sin(x_2) dx_2 + \int_0^{\frac{\theta - \pi}{2}} r - r \cos(-x_4 + \theta) dx_4 \right. \\ \left. + \int_{\theta - \frac{\pi}{2}}^{\frac{3\pi}{2} - \frac{\alpha}{2}} r dx_4 + \int_{\frac{3\pi}{2} - \frac{\alpha}{2}}^{\theta} r - r \cos(x_4) dx_4 + \int_{\frac{\theta}{2}}^{\frac{\pi}{2}} 2r \sin\left(\frac{\theta}{2}\right) \sin(x_2) dx_2 \right) \quad (\text{A.17})$$

$$\bar{p}_{\text{NW2}} = \frac{r}{\pi} \left(\theta - \cos\left(\frac{\alpha}{2}\right) + 1 \right) \quad (\text{A.18})$$

A.2.7.2 Model NW3

NW3 is bounded by $\alpha \leq 3\pi - 2\theta$, $\alpha \geq 2\pi - \theta$ and $\theta \geq \pi/2$ (Fig. 5.2).

NW3 does not have the fourth integral from NW2 as animals are not detectable to the right of the sensor until after the x_4 region has ended and the x_2 region has begun. Therefore the second x_4 integral has an upper limit of θ and the profile after has a width of $r \cos(x_2 - \theta/2)$ and is integrated with respect to x_2 . The final integral starts at $x_4 = 3\pi/2 - \alpha/2 - \theta/2$ and has the full width of $2r \sin(x_2) \sin(\theta/2)$.

$$\bar{p}_{\text{NW3}} = \frac{1}{\pi} \left(\int_{\frac{\theta}{2}}^{\frac{\pi}{2}} 2r \sin\left(\frac{\theta}{2}\right) \sin(x_2) \, dx_2 + \int_0^{\theta - \frac{\pi}{2}} r - r \cos(-x_4 + \theta) \, dx_4 \right. \\ \left. + \int_{\theta - \frac{\pi}{2}}^{\theta} r \, dx_4 + \int_{\frac{\theta}{2}}^{\frac{3\pi}{2} - \frac{\theta}{2} - \frac{\alpha}{2}} r \cos\left(\frac{\theta}{2} - x_2\right) \, dx_2 + \int_{\frac{3\pi}{2} - \frac{\theta}{2} - \frac{\alpha}{2}}^{\frac{\pi}{2}} 2r \sin\left(\frac{\theta}{2}\right) \sin(x_2) \, dx_2 \right) \quad (\text{A.19})$$

$$\bar{p}_{\text{NW3}} = \frac{r}{\pi} \left(\theta - \cos\left(\frac{\alpha}{2}\right) + 1 \right) \quad (\text{A.20})$$

A.2.7.3 Model NW4

Finally, NW4 is bounded by $\alpha \geq \pi$, $\theta \geq \pi/2$ and $\alpha \leq 2\pi - \theta$ (Fig. 5.2). NW4 is the same as NW3 except that the final profile width is zero and this profile is reached at $\alpha/2 + \theta/2 - \pi/2$.

$$\bar{p}_{\text{NW4}} = \frac{1}{\pi} \left(\int_{\frac{\theta}{2}}^{\frac{\pi}{2}} 2r \sin\left(\frac{\theta}{2}\right) \sin(x_2) \, dx_2 + \int_0^{\theta - \frac{\pi}{2}} r - r \cos(-x_4 + \theta) \, dx_4 \right. \\ \left. + \int_{\theta - \frac{\pi}{2}}^{\theta} r \, dx_4 + \int_{\frac{\theta}{2}}^{\frac{\alpha}{2} + \frac{\theta}{2} - \frac{\pi}{2}} r \cos\left(\frac{\theta}{2} - x_2\right) \, dx_2 \right) \quad (\text{A.21})$$

$$\bar{p}_{\text{NW4}} = \frac{r}{\pi} \left(\theta - \cos\left(\frac{\alpha}{2}\right) + 1 \right) \quad (\text{A.22})$$

A.2.8 Model REM

REM is the model from [35]. It has $\alpha = 2\pi$ and $\theta \leq \pi/2$ (Fig. 5.2). It has three profile widths, two of which are repeated, once as the animal approaches from in front of the sensor and once as the animal approaches from behind the sensor.

1. Starting with an approach direction of directly towards the sensor, and examining focal angle x_2 , the profile width is $2r \sin(x_2) \sin(\theta/2)$.
2. When the profile is perpendicular to the radius on the right hand of the sector sensor region, we instead examine x_3 where the profile width is $r \sin(x_3)$.
3. At $x_3 = \pi/2$ the profile becomes simply r and this continues for θ radians of x_4 .
4. The x_3 profile is then repeated with an approach direction from behind the sensor.
5. Finally the x_2 profile is repeated, again with an approach direction from behind the sensor.

$$\bar{p}_{\text{REM}} = \frac{1}{\pi} \left(\int_{\frac{\pi}{2}-\frac{\theta}{2}}^{\frac{\pi}{2}} 2r \sin\left(\frac{\theta}{2}\right) \sin(x_2) dx_2 + \int_{\theta}^{\frac{\pi}{2}} r \sin(x_3) dx_3 \right. \\ \left. + \int_0^{\theta} r dx_4 + \int_{\theta}^{\frac{\pi}{2}} r \sin(x_3) dx_3 + \int_{\frac{\pi}{2}-\frac{\theta}{2}}^{\frac{\pi}{2}} 2r \sin\left(\frac{\theta}{2}\right) \sin(x_2) dx_2 \right) \quad (\text{A.23})$$

$$\bar{p}_{\text{REM}} = \frac{r}{\pi} (\theta + 2) \quad (\text{A.24})$$

A.2.9 Models NW5–7

In the models NW5–7, the sensor has $\theta \leq \pi/2$ as in the REM. As $\alpha \geq \pi$ a lot of the profiles are similar to the REM. Specifically, the first three profiles are always the same as the first three profiles of the REM. This is because when an animal is moving towards the sensor, the $\alpha \geq \pi$ signal is no different to a 2π signal. However, when approaching the sensor from behind, things are slightly different. The animal can only be detected by the sensor if the signal width is large enough that it can be detected once it has passed the sensor.

1. Starting with an approach direction of directly towards the sensor, and examining focal angle x_2 , the profile width is $2r \sin(x_2) \sin(\theta/2)$.
2. When the profile is perpendicular to the radius edge of the sector sensor region, we instead examine x_3 where the profile width is $r \sin(x_3)$.
3. At $x_3 = \pi/2$ the profile becomes simply r and this continues for θ radians of x_4 .
4. If $\alpha \leq 2\pi + 2\theta$, the animal becomes undetectable during this profile when x_3 has decreased in size to $\pi - \alpha/2$. This inequality marks the boundary between NW7 and NW6.
5. If instead $\alpha \geq 2\pi + 2\theta$ then the animal does not become undetectable during the x_3 focal angle. Instead the profile has width greater than zero for the whole of the x_3 angle. The x_2 profile starts with width $r \cos(x_2 - \theta/2)$ as only animals approaching to the left of the sensor are detectable.
6. During this second x_2 profile the signal width needed for animals to be detected to the left of the detector is increasing while the angle needed for animals to be detected to the right of the detector is decreasing. Therefore, either the left side becomes undetectable, making both sides undetectable (this occurs if $\alpha \leq 2\pi - \theta$ as in NW6)

7. or the right becomes detectable (if $\alpha \geq 2\pi - \theta$ as in NW5), making both sides detectable and giving a profile width of $2r \sin(x_2) \sin(\theta/2)$.

A.2.9.1 Model NW5

NW5 is bounded by $\alpha \geq 2\pi - \theta$, $\alpha \leq 2\pi$ and $\theta \leq \pi/2$ (Fig. 5.2).

It is the same as REM except that it includes the extra profile in x_2 (the fifth integral) where only animals approaching to the left of the profile are detected.

$$\begin{aligned} \bar{p}_{\text{NW5}} = \frac{1}{\pi} & \left(\int_{\frac{\pi}{2}-\frac{\theta}{2}}^{\frac{\pi}{2}} 2r \sin\left(\frac{\theta}{2}\right) \sin(x_2) dx_2 + \int_{\theta}^{\frac{\pi}{2}} r \sin(x_3) dx_3 + \int_0^{\theta} r dx_4 \right. \\ & \left. + \int_{\theta}^{\frac{\pi}{2}} r \sin(x_3) dx_3 + \int_{\frac{\pi}{2}-\frac{\theta}{2}}^{\frac{3\pi}{2}-\frac{\theta}{2}-\frac{\alpha}{2}} r \cos\left(\frac{\theta}{2} - x_2\right) dx_2 + \int_{\frac{3\pi}{2}-\frac{\theta}{2}-\frac{\alpha}{2}}^{\frac{\pi}{2}} 2r \sin\left(\frac{\theta}{2}\right) \sin(x_2) dx_2 \right) \end{aligned} \quad (\text{A.25})$$

$$\bar{p}_{\text{NW5}} = \frac{r}{\pi} \left(\theta - \cos\left(\frac{\alpha}{2}\right) + 1 \right) \quad (\text{A.26})$$

A.2.9.2 Model NW6

NW6 is bounded by $\alpha \leq 2\pi - \theta$, $\alpha \geq 2\pi + 2\theta$ and $\theta \leq \pi/2$ (Fig. 5.2).

NW6 is the same NW5 except that as $\alpha \leq 2\pi - \theta$, animals that approach from directly behind the detector are not detected. Therefore at $x_2 = \alpha/2 + \theta/2 - \pi/2$ the profile width goes to zero and therefore the last integral in NW5 is not included.

$$\begin{aligned} \bar{p}_{\text{NW6}} = \frac{1}{\pi} & \left(\int_{\frac{\pi}{2}-\frac{\theta}{2}}^{\frac{\pi}{2}} 2r \sin\left(\frac{\theta}{2}\right) \sin(x_2) dx_2 + \int_{\theta}^{\frac{\pi}{2}} r \sin(x_3) dx_3 \right. \\ & \left. + \int_0^{\theta} r dx_4 + \int_{\theta}^{\frac{\pi}{2}} r \sin(x_3) dx_3 + \int_{\frac{\pi}{2}-\frac{\theta}{2}}^{\frac{\alpha}{2}+\frac{\theta}{2}-\frac{\pi}{2}} r \cos\left(\frac{\theta}{2} - x_2\right) dx_2 \right) \end{aligned} \quad (\text{A.27})$$

$$\bar{p}_{\text{NW6}} = \frac{r}{\pi} \left(\theta - \cos\left(\frac{\alpha}{2}\right) + 1 \right) \quad (\text{A.28})$$

A.2.9.3 Model NW7

NW7 is bounded by $\alpha \geq 2\pi + 2\theta$, $\alpha \geq \pi$ and $\theta \geq 0$ (Fig. 5.2).

It is similar to NW6 but does not include the last integral as during the x_3 profile, at $x_3 = \pi - \alpha/2$ the signal width is too small for any animals to be detected, so the profile width goes to zero.

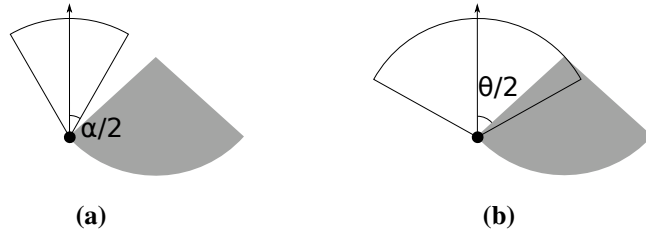


Figure A.6: The first profile in SW models is limited by either α or β depending on whether $\alpha < \beta$. The sector shaped detection region is shown in grey. Animals are filled black circles and the animal signal is an unfilled sector. The animals direction of movement is indicated with an arrow. (a) As $\alpha/2 < \theta/2$ the profile width is limited by the signal width rather than the sensor region. The profile width is $2r \sin(\alpha/2)$ (b) As $\alpha/2 > \theta/2$ the profile width is limited by the sensor region, not the signal width. The profile width is $2r \sin(\theta/2) \sin(x_2)$.

$$\bar{p}_{NW7} = \frac{1}{\pi} \left(\int_{\frac{\pi}{2} - \frac{\theta}{2}}^{\frac{\pi}{2}} 2r \sin\left(\frac{\theta}{2}\right) \sin(x_2) dx_2 + \int_{\theta}^{\frac{\pi}{2}} r \sin(x_3) dx_3 + \int_0^{\theta} r dx_4 + \int_{\pi - \frac{\alpha}{2}}^{\frac{\pi}{2}} r \sin(x_3) dx_3 \right) \quad (\text{A.29})$$

$$\bar{p}_{NW7} = \frac{r}{\pi} \left(\theta - \cos\left(\frac{\alpha}{2}\right) + 1 \right) \quad (\text{A.30})$$

A.2.10 Model SW1–3

The models in SW1–3 are described with the two focal angles used in models NW2–4, x_2 and x_4 . As $\alpha \leq \pi$ an animal can never be detected if it is approaching the detector from behind. This makes these models simpler in that they go through the x_2 and x_4 profiles only once each.

There are five potential profile sizes.

1. At the beginning of x_2 , with an approach direction directly towards the sensor, the parameter that limits the width of the profile can either be the sensor width, in which case the profile width is $2r \sin(\theta/2) \sin(x_2)$.
2. Or the signal width can be the limiting parameter, in which case the profile width is instead $2r \sin(\alpha/2)$ (Fig. A.6)
3. The next potential profile in x_2 has a width of $r \sin(\alpha/2) - r \cos(x_2 + \theta/2)$ as the right side of the profile is limited by the width of the sensor region while the left side is limited by the signal width. However, the angle at which the profile starts depends on whether the first profile was 1) or 2) above. If the first profile is profile 1) then the profile is limited

on both sides by the sensor region and then the left side of the profile becomes limited by the signal width. This happens at $x_2 = \pi/2 - \alpha/2 + \theta/2$. If however the first profile was 2) then the first profile is limited by the signal width. We move into the new profile when the right side of the profile becomes limited by the sensor region. This occurs at $x_2 = \pi/2 + \alpha/2 - \theta/2$.

4. In the x_4 region the left side of the profile is always $r \sin(\alpha/2)$ while the right side is either 0, giving a profile of $r \sin(\alpha/2)$.
5. Or limited by the sensor giving a profile of size $r \sin(\alpha/2) - r \cos(x_4 - \theta)$.

A.2.10.1 Model SW1

SW1 is bounded by $\alpha \geq \theta$, $\alpha \leq \pi$ and $\theta \leq \pi$ (Fig. 5.2).

As α is large the first profile is limited by the size of the sensor region giving it a width of $2r \sin(\theta/2) \sin(x_2)$. It is the only one of the three SW models to start in this way. Later on, still with x_2 as the focal angle the left side of the profile does become limited by the signal width. So at $x_2 = \pi/2 - \alpha/2 + \theta/2$ the profile width becomes $r \sin(\alpha/2) - r \cos(x_2 + \theta/2)$.

As we enter the x_4 region, the profile remains limited by the signal on the left and by the sensor on the right, giving a profile width of $r \sin(\alpha/2) - r \cos(x_4 - \theta)$. Finally, at $x_4 = \theta - \pi/2$ the right side of the profile becomes zero and the profile is width is $r \sin(\alpha/2)$.

$$\bar{p}_{\text{SW1}} = \frac{1}{\pi} \left(\int_{\frac{\pi}{2} + \frac{\theta}{2} - \frac{\alpha}{2}}^{\frac{\pi}{2}} 2r \sin\left(\frac{\theta}{2}\right) \sin(x_2) dx_2 + \int_{\frac{\theta}{2}}^{\frac{\pi}{2} + \frac{\theta}{2} - \frac{\alpha}{2}} r \sin\left(\frac{\alpha}{2}\right) - r \cos\left(\frac{\theta}{2} + x_2\right) dx_2 \right. \\ \left. + \int_0^{\theta - \frac{\pi}{2}} r \sin\left(\frac{\alpha}{2}\right) - r \cos(\theta - x_4) dx_4 + \int_{\theta - \frac{\pi}{2}}^{\frac{\alpha}{2} + \theta - \frac{\pi}{2}} r \sin\left(\frac{\alpha}{2}\right) dx_4 \right) \quad (\text{A.31})$$

$$\bar{p}_{\text{SW1}} = \frac{r}{\pi} \left(\theta \sin\left(\frac{\alpha}{2}\right) - \cos\left(\frac{\alpha}{2}\right) + 1 \right) \quad (\text{A.32})$$

A.2.10.2 Model SW2

SW2 is bounded by $\theta \geq \pi/2$, $\alpha \leq \theta$ and $\alpha \geq 2\theta - \pi$ (Fig. 5.2).

SW2 is largely similar to SW1. However, as $\alpha \leq \theta$ the first profile is limited by α and not by the detection region. Therefore the first profile has width $2r \sin(\alpha/2)$. This also means the transition to the second profile occurs at $x_2 = \pi/2 + \alpha/2 - \theta/2$ instead of $x_2 = \pi/2 - \alpha/2 + \theta/2$.

$$\bar{p}_{\text{SW2}} = \frac{1}{\pi} \left(\int_{\frac{\alpha}{2} - \frac{\theta}{2} + \frac{\pi}{2}}^{\frac{\pi}{2}} 2r \sin\left(\frac{\alpha}{2}\right) dx_2 + \int_{\frac{\theta}{2}}^{\frac{\alpha}{2} - \frac{\theta}{2} + \frac{\pi}{2}} r \sin\left(\frac{\alpha}{2}\right) - r \cos\left(\frac{\theta}{2} + x_2\right) dx_2 \right. \\ \left. + \int_0^{\theta - \frac{\pi}{2}} r \sin\left(\frac{\alpha}{2}\right) - r \cos(\theta - x_4) dx_4 + \int_{\theta - \frac{\pi}{2}}^{\frac{\alpha}{2} + \theta - \frac{\pi}{2}} r \sin\left(\frac{\alpha}{2}\right) dx_4 \right) \quad (\text{A.33})$$

$$\bar{p}_{\text{SW2}} = \frac{r}{\pi} \left(\theta \sin\left(\frac{\alpha}{2}\right) - \cos\left(\frac{\alpha}{2}\right) + 1 \right) \quad (\text{A.34})$$

A.2.10.3 Model SW3

SW3 is bounded by $\alpha \leq 2\theta - \pi$ and $\theta \leq \pi$ (Fig. 5.2).

SW3 is similar to SW2 except that the profile does not become limited by sensor at all during the the x_4 regions. Therefore, at $x_4 = 0$ the profile is still of width $2r \sin(\alpha/2)$. Only at $x_4 = \theta - \pi/2 - \alpha/2$ does the profile become limited on the right by the sensor region.

$$\bar{p}_{\text{SW3}} = \frac{1}{\pi} \left(\int_{\frac{\theta}{2}}^{\frac{\pi}{2}} 2r \sin\left(\frac{\alpha}{2}\right) dx_2 + \int_0^{-\frac{\pi}{2} + \theta - \frac{\alpha}{2}} 2r \sin\left(\frac{\alpha}{2}\right) dx_4 \right. \\ \left. + \int_{-\frac{\pi}{2} + \theta - \frac{\alpha}{2}}^{\theta - \frac{\pi}{2}} r \sin\left(\frac{\alpha}{2}\right) - r \cos(\theta - x_4) dx_4 + \int_{\theta - \frac{\pi}{2}}^{\frac{\alpha}{2} + \theta - \frac{\pi}{2}} r \sin\left(\frac{\alpha}{2}\right) dx_4 \right) \quad (\text{A.35})$$

$$\bar{p}_{\text{SW3}} = \frac{r}{\pi} \left(\theta \sin\left(\frac{\alpha}{2}\right) - \cos\left(\frac{\alpha}{2}\right) + 1 \right) \quad (\text{A.36})$$

A.2.11 Model SW4-9

As $\alpha < \pi$, animals approaching the sensor from behind can never be detected, so unlike REM, the second x_2 and x_3 profiles are always zero. The six models are split by three inequalities that relate to the models as follows.

1. Models with $\alpha \leq \pi - 2\theta$ have no x_4 profile. This is because at $x_4 = 0$, the signal width is already too small to be detected as can be seen in Fig. A.7a where $\alpha/2 < \pi/2 - \theta$ which simplifies to give the previous inequality.
2. Models with $\alpha \leq \theta$ are limited by α in the first, x_2 region (Fig. A.6), rather than being limited by θ . Therefore this first profile is of width $2r \sin(\alpha/2)$ rather than $2r \sin(\theta/2) \sin(x_2)$.
3. Finally, models with $\alpha \leq 2\theta$ have a second profile in x_2 where to one side of the sensor

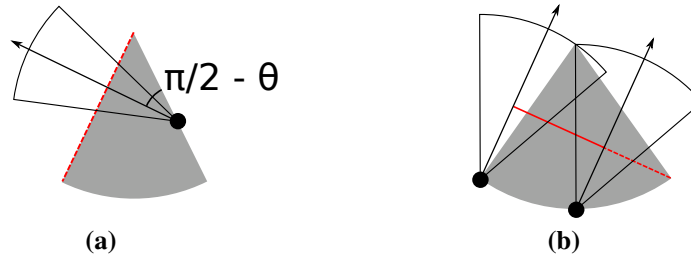


Figure A.7: Description of two profiles in SW models. The sector shaped detection region is shown in grey. Animals are filled black circles and the animal signal is an unfilled sector. The animals direction of movement is indicated with an arrow. The profile p is shown with a red line. Dashed red lines indicate areas where animals cannot be detected. (a) At $x_4 = 0$, if $\alpha/2 < \pi/2 - \theta$ then $\alpha/2$ is too small for an animal to be detected at all during the x_4 profile (shown with dashed red.) This inequality simplifies to $\alpha < \pi - 2\theta$. (b) The right of the profile is limited by the signal width, not the sensor. On the left, the profile is limited by the sensor and not the signal. Overall the profile width is $r \sin(\alpha/2) - r \cos(x_2 + \theta/2)$.

α is the limiting factor of profile width, while on the other side θ is (Fig. A.7b). This gives a width of $r \sin(\alpha/2) - r \cos(x_2 + \theta/2)$. This profile does not occur in models with $\alpha \geq 2\theta$.

A.2.11.1 Model SW4

SW4 is bounded by $\alpha \leq \theta$, $\alpha \geq \pi - 2\theta$ and $\theta \leq \pi/2$ (Fig. 5.2). Therefore it does contain a x_4 profile, starts with an α limited profile and does contain the $r \sin(\alpha/2) - r \cos(x_2 + \theta/2)$ profile in x_2 .

$$\bar{p}_{\text{SW4}} = \frac{1}{\pi} \left(\int_{\frac{\alpha}{2} - \frac{\theta}{2} + \frac{\pi}{2}}^{\frac{\pi}{2}} 2r \sin\left(\frac{\alpha}{2}\right) dx_2 + \int_{\frac{\pi}{2} - \frac{\theta}{2}}^{\frac{\alpha}{2} - \frac{\theta}{2} + \frac{\pi}{2}} r \sin\left(\frac{\alpha}{2}\right) - r \cos\left(\frac{\theta}{2} + x_2\right) dx_2 \right. \\ \left. + \int_{\theta}^{\frac{\pi}{2}} r \sin\left(\frac{\alpha}{2}\right) dx_3 + \int_0^{\frac{\alpha}{2} + \theta - \frac{\pi}{2}} r \sin\left(\frac{\alpha}{2}\right) dx_4 \right) \quad (\text{A.37})$$

$$\bar{p}_{\text{SW4}} = \frac{r}{\pi} \left(\theta \sin\left(\frac{\alpha}{2}\right) - \cos\left(\frac{\alpha}{2}\right) + 1 \right) \quad (\text{A.38})$$

A.2.11.2 Model SW5

SW5 is the only model with a tetrahedral bounding region. It is bounded by $\alpha \geq \theta$, $\alpha \geq \pi - 2\theta$, $\alpha \leq 2\theta$ and $\theta \leq \pi/2$ (Fig. 5.2). Therefore it does contain a x_4 profile, but starts with a θ limited profile. It does contain the $r \sin(\alpha/2) - r \cos(x_2 + \theta/2)$ profile in x_2 .

$$\bar{p}_{\text{sw5}} = \frac{1}{\pi} \left(\int_{\frac{\pi}{2} + \frac{\theta}{2} - \frac{\alpha}{2}}^{\frac{\pi}{2}} 2r \sin\left(\frac{\theta}{2}\right) \sin(x_2) \, dx_2 + \int_{\frac{\pi}{2} - \frac{\theta}{2}}^{\frac{\pi}{2} + \frac{\theta}{2} - \frac{\alpha}{2}} r \sin\left(\frac{\alpha}{2}\right) - r \cos\left(\frac{\theta}{2} + x_2\right) \, dx_2 \right. \\ \left. + \int_{\theta}^{\frac{\pi}{2}} r \sin\left(\frac{\alpha}{2}\right) \, dx_3 + \int_0^{\frac{\alpha}{2} + \theta - \frac{\pi}{2}} r \sin\left(\frac{\alpha}{2}\right) \, dx_4 \right) \quad (\text{A.39})$$

$$\bar{p}_{\text{sw5}} = \frac{r}{\pi} \left(\theta \sin\left(\frac{\alpha}{2}\right) - \cos\left(\frac{\alpha}{2}\right) + 1 \right) \quad (\text{A.40})$$

A.2.11.3 Model SW6

SW6 is bounded by $\alpha \geq \pi - 2\theta$, $\alpha \geq 2\theta$ and $\alpha \leq \pi$ (Fig. 5.2). It starts with a θ limited profile and has a x_4 profile. However, it does not contain the $r \sin(\alpha/2) - r \cos(x_2 + \theta/2)$ profile.

$$\bar{p}_{\text{sw6}} = \frac{1}{\pi} \left(\int_{\frac{\pi}{2} - \frac{\theta}{2}}^{\frac{\pi}{2}} 2r \sin\left(\frac{\theta}{2}\right) \sin(x_2) \, dx_2 + \int_{\theta}^{\frac{\alpha}{2}} r \sin(x_3) \, dx_3 \right. \\ \left. + \int_{\frac{\alpha}{2}}^{\frac{\pi}{2}} r \sin\left(\frac{\alpha}{2}\right) \, dx_3 + \int_0^{\frac{\alpha}{2} + \theta - \frac{\pi}{2}} r \sin\left(\frac{\alpha}{2}\right) \, dx_4 \right) \quad (\text{A.41})$$

$$\bar{p}_{\text{sw6}} = \frac{r}{\pi} \left(\theta \sin\left(\frac{\alpha}{2}\right) - \cos\left(\frac{\alpha}{2}\right) + 1 \right) \quad (\text{A.42})$$

A.2.11.4 Model SW7

SW7 is bounded by $\alpha \leq \pi - 2\theta$, $\alpha \leq \theta$ and $\alpha < 0$ (Fig. 5.2). Therefore it does not contain a x_4 profile. It starts with an α limited profile and contains the $r \sin(\alpha/2) - r \cos(x_2 + \theta/2)$ profile in x_2 .

$$\bar{p}_{\text{sw7}} = \frac{1}{\pi} \left(\int_{\frac{\alpha}{2} - \frac{\theta}{2} + \frac{\pi}{2}}^{\frac{\pi}{2}} 2r \sin\left(\frac{\alpha}{2}\right) \, dx_2 + \int_{\frac{\pi}{2} - \frac{\theta}{2}}^{\frac{\alpha}{2} - \frac{\theta}{2} + \frac{\pi}{2}} r \sin\left(\frac{\alpha}{2}\right) - r \cos\left(\frac{\theta}{2} + x_2\right) \, dx_2 + \int_{\theta}^{\frac{\alpha}{2} + \theta} r \sin\left(\frac{\alpha}{2}\right) \, dx_3 \right) \quad (\text{A.43})$$

$$\bar{p}_{\text{sw7}} = \frac{r}{\pi} \left(\theta \sin\left(\frac{\alpha}{2}\right) - \cos\left(\frac{\alpha}{2}\right) + 1 \right) \quad (\text{A.44})$$

A.2.11.5 Model SW8

SW8 is bounded by $\alpha \leq \pi - 2\theta$, $\alpha \geq \theta$ and $\alpha \leq 2\theta$ (Fig. 5.2). It starts with a θ limited profile. It does contain the $r \sin(\alpha/2) - r \cos(x_2 + \theta/2)$ profile in x_2 but does not have a x_4 profile.

$$\bar{p}_{\text{sw8}} = \frac{1}{\pi} \left(\int_{\frac{\pi}{2} + \frac{\theta}{2} - \frac{\alpha}{2}}^{\frac{\pi}{2}} 2r \sin\left(\frac{\theta}{2}\right) \sin(x_2) \, dx_2 + \int_{\frac{\pi}{2} - \frac{\theta}{2}}^{\frac{\pi}{2} + \frac{\theta}{2} - \frac{\alpha}{2}} r \sin\left(\frac{\alpha}{2}\right) - r \cos\left(\frac{\theta}{2} + x_2\right) \, dx_2 + \int_{\theta}^{\frac{\alpha}{2} + \theta} r \sin\left(\frac{\alpha}{2}\right) \, dx_3 \right) \quad (\text{A.45})$$

$$\bar{p}_{\text{sw8}} = \frac{r}{\pi} \left(\theta \sin\left(\frac{\alpha}{2}\right) - \cos\left(\frac{\alpha}{2}\right) + 1 \right) \quad (\text{A.46})$$

A.2.11.6 Model SW9

Finally, SW9, the last model, is bounded by $\alpha \leq \pi - 2\theta$, $\alpha \geq 2\theta$ and $\theta \geq 0$ (Fig. 5.2). Therefore it starts with a θ limited profile. However it does not contain the extra x_2 profile nor a x_4 profile.

$$\bar{p}_{\text{sw9}} = \frac{1}{\pi} \left(\int_{\frac{\pi}{2} - \frac{\theta}{2}}^{\frac{\pi}{2}} 2r \sin\left(\frac{\theta}{2}\right) \sin(x_2) \, dx_2 + \int_{\theta}^{\frac{\alpha}{2}} r \sin(x_3) \, dx_3 + \int_{\frac{\alpha}{2}}^{\frac{\alpha}{2} + \theta} r \sin\left(\frac{\alpha}{2}\right) \, dx_3 \right) \quad (\text{A.47})$$

$$\bar{p}_{\text{sw9}} = \frac{r}{\pi} \left(\theta \sin\left(\frac{\alpha}{2}\right) - \cos\left(\frac{\alpha}{2}\right) + 1 \right) \quad (\text{A.48})$$

A.3 Supplementary Information: Simulation model results of the gREM precision

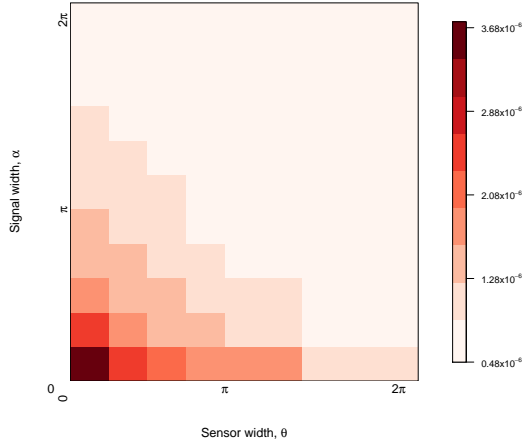


Figure A.1: Simulation model results of the gREM precision given a range of sensor and signal widths, shown by the standard deviation of the error between the estimated and true densities. Standard deviations are shown from deep red to pink, representing high to low values between 0.483×10^{-6} to 3.74×10^{-6} .

A.4 Supplementary Information: Impact of parameter error

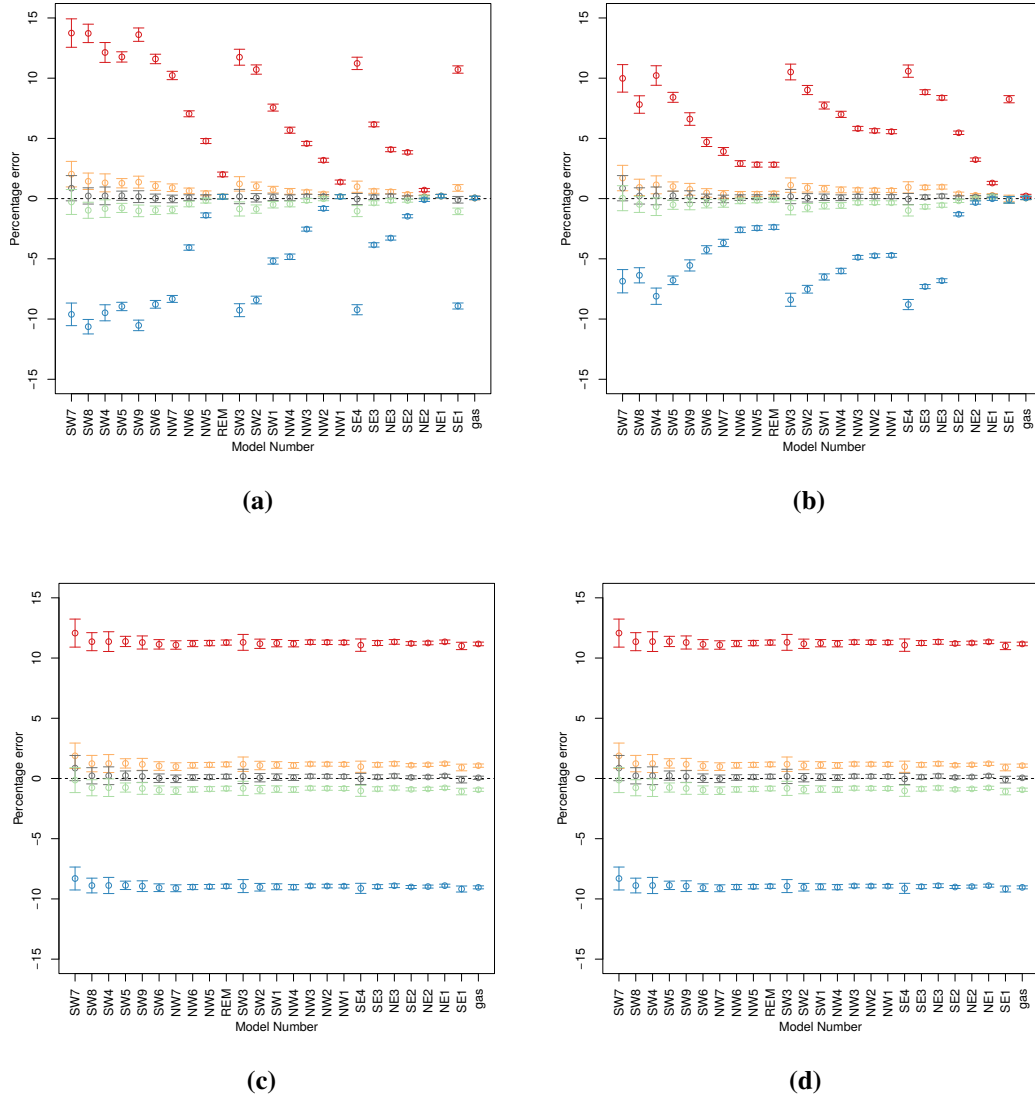


Figure A.1: Model sensitivity (for all gREM submodels) to error in estimates of a) signal width α , b) sensor width θ , c) detection distance r and d) animal movement speed v . Estimates are -10% (red), -1% (orange), 0% (grey), +1% (green) and +10% (blue) of the true parameter value. The black dashed line indicates zero error in density estimates. The error bars 95% confidence intervals across all simulations.

Appendix B

Colophon

This is a description of the tools you used to make your thesis. It helps people make future documents, reminds you, and looks good.

(example) This document was set in the Times Roman typeface using L^AT_EX and BibT_EX, composed with a text editor.

Bibliography

- [1] Kate E Jones, Nikkita G Patel, Marc A Levy, Adam Storeygard, Deborah Balk, John L Gittleman, and Peter Daszak. Global trends in emerging infectious diseases. *Nature*, 451(7181):990–993, 2008.
- [2] Tsukushi Kamiya, Katie O’Dwyer, Shinichi Nakagawa, and Robert Poulin. What determines species richness of parasitic organisms? a meta-analysis across animal, plant and fungal hosts. *Biological Reviews*, 89(1):123–134, 2014.
- [3] Hans J Bremermann and HR Thieme. A competitive exclusion principle for pathogen virulence. *Journal of mathematical biology*, 27(2):179–190, 1989.
- [4] Maia Martcheva and Xue-Zhi Li. Competitive exclusion in an infection-age structured model with environmental transmission. *Journal of Mathematical Analysis and Applications*, 408(1):225–246, 2013.
- [5] Azmy S Ackleh and Linda JS Allen. Competitive exclusion and coexistence for pathogens in an epidemic model with variable population size. *Journal of mathematical biology*, 47(2):153–168, 2003.
- [6] Azmy S Ackleh and Paul L Salceanu. Robust uniform persistence and competitive exclusion in a nonautonomous multi-strain sir epidemic model with disease-induced mortality. *Journal of mathematical biology*, 68(1-2):453–475, 2014.
- [7] KME Turner and GP Garnett. The impact of the phase of an epidemic of sexually transmitted infection on the evolution of the organism. *Sexually transmitted infections*, 78:i20–i30, 2002.
- [8] Chiara Poletto, Sandro Meloni, Vittoria Colizza, Yamir Moreno, and Alessandro Vespignani. Host mobility drives pathogen competition in spatially structured populations. *PLoS computational biology*, 9(8):e1003169, 2013.

- [9] Chiara Poletto, Sandro Meloni, Ashleigh Van Metre, Vittoria Colizza, Yamir Moreno, and Alessandro Vespignani. Characterising two-pathogen competition in spatially structured environments. *Scientific reports*, 5, 2015.
- [10] Brian Karrer and MEJ Newman. Competing epidemics on complex networks. *Physical Review E*, 84(3):036106, 2011.
- [11] Gaël D Maganga, Mathieu Bourgarel, Peter Vallo, Thierno D Dallo, Carine Ngoagouni, Jan Felix Drexler, Christian Drosten, Emmanuel R Nakouné, Eric M Leroy, and Serge Morand. Bat distribution size or shape as determinant of viral richness in african bats. *PloS one*, 9(6):e100172, 2014.
- [12] Noellie Gay, Kevin J Olival, Sara Bumrungsri, Boripat Siriaronrat, Mathieu Bourgarel, and Serge Morand. Parasite and viral species richness of southeast asian bats: Fragmentation of area distribution matters. *International Journal for Parasitology: Parasites and Wildlife*, 3(2):161–170, 2014.
- [13] Amy S Turmelle and Kevin J Olival. Correlates of viral richness in bats (order chiroptera). *EcoHealth*, 6(4):522–539, 2009.
- [14] C.H. Calisher, J.E. Childs, H.E. Field, K.V. Holmes, and T. Schountz. Bats: important reservoir hosts of emerging viruses. *Clinical Microbiology Reviews*, 19(3):531–545, 2006.
- [15] James M Hughes, Mary E Wilson, Kim Halpin, Alexander D Hyatt, Raina K Plowright, Jonathan H Epstein, Peter Daszak, Hume E Field, Linfa Wang, Peter W Daniels, et al. Emerging viruses: coming in on a wrinkled wing and a prayer. *Clinical Infectious Diseases*, 44(5):711–717, 2007.
- [16] Wendong Li, Zhengli Shi, Meng Yu, Wuze Ren, Craig Smith, Jonathan H Epstein, Hanzhong Wang, Gary Crameri, Zhihong Hu, Huajun Zhang, et al. Bats are natural reservoirs of sars-like coronaviruses. *Science*, 310(5748):676–679, 2005.
- [17] Kate E Jones, Jon Bielby, Marcel Cardillo, Susanne A Fritz, Justin O’Dell, C David L Orme, Kamran Safi, Wes Sechrest, Elizabeth H Boakes, Chris Carbone, et al. PanTHERIA: a species-level database of life history, ecology, and geography of extant and recently extinct mammals: Ecological archives e090-184. *Ecology*, 90(9):2648–2648, 2009.
- [18] S Joseph Wright and Stephen P Hubbell. Stochastic extinction and reserve size: a focal species approach. *Oikos*, pages 466–476, 1983.

- [19] Andy Purvis, John L Gittleman, Guy Cowlshaw, and Georgina M Mace. Predicting extinction risk in declining species. *Proceedings of the Royal Society of London. Series B: Biological Sciences*, 267(1456):1947–1952, 2000.
- [20] Kristoffer T Everatt, Leah Andresen, and Michael J Somers. Trophic scaling and occupancy analysis reveals a lion population limited by top-down anthropogenic pressure in the Limpopo National Park, Mozambique. *PloS one*, 9(6):e99389, 2014.
- [21] KU Karanth. Estimating tiger (*Panthera tigris*) populations from camera-trap data using capture–recapture models. *Biological Conservation*, 71(3):333–338, 1995.
- [22] J Marcus Rowcliffe and Chris Carbone. Surveys using camera traps: are we looking to a brighter future? *Animal Conservation*, 11(3):185–186, 2008.
- [23] Miguel A Acevedo and Luis J Villanueva-Rivera. Using automated digital recording systems as effective tools for the monitoring of birds and amphibians. *Wildlife Society Bulletin*, 34(1):211–214, 2006.
- [24] Charlotte L Walters, Robin Freeman, Alanna Collen, Christian Dietz, M Brock Fenton, Gareth Jones, Martin K Obrist, Sébastien J Puechmaille, Thomas Sattler, Björn M Siemers, et al. A continental-scale tool for acoustic identification of European bats. *Journal of Applied Ecology*, 49(5):1064–1074, 2012.
- [25] ST Kessel, SJ Cooke, MR Heupel, NE Hussey, CA Simpfendorfer, S Vagle, and AT Fisk. A review of detection range testing in aquatic passive acoustic telemetry studies. *Reviews in Fish Biology and Fisheries*, 24(1):199–218, 2014.
- [26] Charlotte L Walters, Alanna Collen, Tim Lucas, Kim Mroz, Catherine A Sayer, and Kate E Jones. Challenges of using bioacoustics to globally monitor bats. In Rick A. Adams and Scott C. Pedersen, editors, *Bat Evolution, Ecology, and Conservation*, pages 479–499. Springer, 2013.
- [27] David R Anderson. The need to get the basics right in wildlife field studies. *Wildlife Society Bulletin*, 29(4):1294–1297, 2001.
- [28] David Borchers, Greg Distiller, Rebecca Foster, Bart Harmsen, and Lorenzo Milazzo. Continuous-time spatially explicit capture–recapture models, with an application to a jaguar camera-trap survey. *Methods in Ecology and Evolution*, 5(7):656–665, 2014.

- [29] Danielle Harris, Luis Matias, Len Thomas, John Harwood, and Wolfram H Geissler. Applying distance sampling to fin whale calls recorded by single seismic instruments in the northeast Atlantic. *The Journal of the Acoustical Society of America*, 134(5):3522–3535, 2013.
- [30] J. Barlow and B.L. Taylor. Estimates of sperm whale abundance in the northeastern temperate pacific from a combined acoustic and visual survey. *Marine Mammal Science*, 21(3):429–445, 2005.
- [31] Tiago A Marques, Lisa Munger, Len Thomas, Sean Wiggins, and John A Hildebrand. Estimating north pacific right whale *eubalaena japonica* density using passive acoustic cue counting. *Endangered Species Research*, 13(3):163–172, 2011.
- [32] J Andrew Royle and James D Nichols. Estimating abundance from repeated presence-absence data or point counts. *Ecology*, 84(3):777–790, 2003.
- [33] Darryl I MacKenzie and J Andrew Royle. Designing occupancy studies: general advice and allocating survey effort. *Journal of Applied Ecology*, 42(6):1105–1114, 2005.
- [34] Victoria H Zero, Siva R Sundaresan, Timothy G O’Brien, and Margaret F Kinnaird. Monitoring an endangered savannah ungulate, Grevy’s zebra (*Equus grevyi*): choosing a method for estimating population densities. *Oryx*, 47(03):410–419, 2013.
- [35] J.M. Rowcliffe, J. Field, S.T. Turvey, and C. Carbone. Estimating animal density using camera traps without the need for individual recognition. *Journal of Applied Ecology*, 45(4):1228–1236, 2008.
- [36] Anthony Brusa and Daniel E Bunker. Increasing the precision of canopy closure estimates from hemispherical photography: Blue channel analysis and under-exposure. *Agricultural and Forest Meteorology*, 195:102–107, 2014.
- [37] Daniel T Blumstein, Daniel J Mennill, Patrick Clemins, Lewis Girod, Kung Yao, Gail Patricelli, Jill L Deppe, Alan H Krakauer, Christopher Clark, Kathryn A Cortopassi, et al. Acoustic monitoring in terrestrial environments using microphone arrays: applications, technological considerations and prospectus. *Journal of Applied Ecology*, 48(3):758–767, 2011.
- [38] Tracey L Rogers, Michaela B Ciaglia, Holger Klinck, and Colin Southwell. Density can be misleading for low-density species: benefits of passive acoustic monitoring. *Public Library of Science One*, 8(1):e52542, 2013.

- [39] Marianne Marcoux, Marie Auger-Méthé, Elly G Chmelnitsky, Steven H Ferguson, and Murray M Humphries. Local passive acoustic monitoring of narwhal presence in the Canadian Arctic: a pilot project. *Arctic*, 64(3):307–316, 2011.
- [40] Marion Depraetere, Sandrine Pavoine, Frédéric Jiguet, Amandine Gasc, Stéphanie Duvail, and Jérôme Sueur. Monitoring animal diversity using acoustic indices: implementation in a temperate woodland. *Ecological Indicators*, 13(1):46–54, 2012.
- [41] Tiago A Marques, Len Thomas, Stephen W Martin, David K Mellinger, Jessica A Ward, David J Moretti, Danielle Harris, and Peter L Tyack. Estimating animal population density using passive acoustics. *Biological Reviews*, 88(2):287–309, 2013.
- [42] T Lewis, D Gillespie, C Lacey, J Matthews, M Danbolt, R Leaper, R McLanaghan, and A Moscrop. Sperm whale abundance estimates from acoustic surveys of the Ionian Sea and Straits of Sicily in 2003. *Journal of the Marine Biological Association of the United Kingdom*, 87(01):353–357, 2007.
- [43] Stephen T Buckland, Stuart J Marsden, and Rhys E Green. Estimating bird abundance: making methods work. *Bird Conservation International*, 18(S1):S91–S108, 2008.
- [44] Benedikt R Schmidt. Count data, detection probabilities, and the demography, dynamics, distribution, and decline of amphibians. *Comptes Rendus Biologies*, 326:119–124, 2003.
- [45] WB Yapp. The theory of line transects. *Bird study*, 3(2):93–104, 1956.
- [46] John M C Hutchinson and Peter M Waser. Use, misuse and extensions of “ideal gas” models of animal encounter. *Biological Reviews of the Cambridge Philosophical Society*, 82(3):335–359, 2007.
- [47] S. Brinkløv, L. Jakobsen, J.M. Ratcliffe, E.K.V. Kalko, and A. Surlykke. Echolocation call intensity and directionality in flying short-tailed fruit bats, *Carollia perspicillata* (phyllostomidae). *The Journal of the Acoustical Society of America*, 129(1):427–435, 2011.
- [48] Chris Carbone, Guy Cowlishaw, Nick JB Isaac, and J Marcus Rowcliffe. How far do animals go? Determinants of day range in mammals. *The American Naturalist*, 165(2):290–297, 2005.
- [49] MW Holderied and O. Von Helversen. Echolocation range and wingbeat period match in aerial-hawking bats. *Proc. R. Soc. B*, 270(1530):2293–2299, 2003.

- [50] A.M. Adams, M.K. Jantzen, R.M. Hamilton, and M.B. Fenton. Do you hear what I hear? Implications of detector selection for acoustic monitoring of bats. *Methods in Ecology and Evolution*, 2012.
- [51] SymPy Development Team. *SymPy: Python library for symbolic mathematics*, 2014.
- [52] R Development Core Team. *R: A Language And Environment For Statistical Computing*. R Foundation For Statistical Computing, Vienna, Austria, 2010. ISBN 3-900051-07-0.
- [53] John Damuth. Population density and body size in mammals. *Nature*, 290(5808):699–700, 1981.
- [54] Satoko Kimura, Tomonari Akamatsu, Lijun Dong, Kexiong Wang, Ding Wang, Yasutoki Shibata, and Nobuaki Arai. Acoustic capture-recapture method for towed acoustic surveys of echolocating porpoises. *The Journal of the Acoustical Society of America*, 135(6):3364–3370, 2014.
- [55] Kate E Jones, Jon A Russ, Andriy-Taras Bashta, Zoltán Bilhari, Colin Catto, István Csősz, Alexander Gorbachev, Páler Győrfi, Alice Hughes, Igor Ivashkiv, et al. Indicator bats program: a system for the global acoustic monitoring of bats. *Biodiversity Monitoring and Conservation: Bridging the Gap between Global Commitment and Local Action*, pages 211–247, 2011.
- [56] Francesco Rovero, Fridolin Zimmermann, Duccio Berzi, and Paul Meek. “which camera trap type and how many do I need?” A review of camera features and study designs for a range of wildlife research applications. *Hystrix*, 24(2):148–156, 2013.
- [57] Len Thomas and Tiago A Marques. Passive acoustic monitoring for estimating animal density. *Acoustics Today*, 8(3):35–44, 2012.
- [58] Timothy G O’Brien, Margaret F Kinnaird, and Hariyo T Wibisono. Crouching tigers, hidden prey: Sumatran tiger and prey populations in a tropical forest landscape. *Animal Conservation*, 6(2):131–139, 2003.
- [59] Rebecca J Foster and Bart J Harmsen. A critique of density estimation from camera-trap data. *The Journal of Wildlife Management*, 76(2):224–236, 2012.
- [60] Peter E Smouse, Stefano Focardi, Paul R Moorcroft, John G Kie, James D Forester, and Juan M Morales. Stochastic modelling of animal movement. *Philosophical Transactions of the Royal Society B: Biological Sciences*, 365(1550):2201–2211, 2010.

- [61] Stephen T Buckland and CM Handel. Point-transect surveys for songbirds: robust methodologies. *The Auk*, 123(2):345–357, 2006.
- [62] Heather M Hassel-Finnegan, Carola Borries, Eileen Larney, Mayuree Umponjan, and Andreas Koenig. How reliable are density estimates for diurnal primates? *International Journal of Primatology*, 29(5):1175–1187, 2008.
- [63] Enrique A Crespo, Susana N Pedraza, M Florencia Grandi, Silvana L Dans, and Griselda V Garaffo. Abundance and distribution of endangered Franciscana dolphins in Argentine waters and conservation implications. *Marine Mammal Science*, 26(1):17–35, 2010.
- [64] Vitek Jirinec, Brent R Campos, and Matthew D Johnson. Roosting behaviour of a migratory songbird on Jamaican coffee farms: landscape composition may affect delivery of an ecosystem service. *Bird Conservation International*, 21(03):353–361, 2011.
- [65] Marcella J Kelly, Julie Betsch, Claudia Wultsch, Bernardo Mesa, and L Scott Mills. Non-invasive sampling for carnivores. In L Boitani and RA Powell, editors, *Carnivore ecology and conservation: a handbook of techniques*, pages 47–69. Oxford University Press, New York, 2012.